

Hitomi observation of radio galaxy NGC 1275: The first X-ray microcalorimeter spectroscopy of Fe-K α line emission from an active galactic nucleus*

Hitomi Collaboration, Felix AHARONIAN,¹ Hiroki AKAMATSU,²
Fumie AKIMOTO,³ Steven W. ALLEN,^{4,5,6} Lorella ANGELINI,⁷ Marc AUDARD,⁸
Hisamitsu AWAKI,⁹ Magnus AXELSSON,¹⁰ Aya BAMBA,^{11,12}
Marshall W. BAUTZ,¹³ Roger BLANDFORD,^{4,5,6} Laura W. BRENNEMAN,¹⁴
Gregory V. BROWN,¹⁵ Esra BULBUL,¹³ Edward M. CACKETT,¹⁶
Maria CHERNYAKOVA,¹ Meng P. CHIAO,⁷ Paolo S. COPPI,^{17,18}
Elisa COSTANTINI,² Jelle DE PLAA,² Cor P. DE VRIES,² Jan-Willem DEN HERDER,²
Chris DONE,¹⁹ Tadayasu DOTANI,²⁰ Ken EBISAWA,²⁰ Megan E. ECKART,⁷
Teruaki ENOTO,^{21,22} Yuichiro EZOE,²³ Andrew C. FABIAN,²⁴ Carlo FERRIGNO,⁸
Adam R. FOSTER,¹⁴ Ryuichi FUJIMOTO,²⁵ Yasushi FUKAZAWA,²⁶
Akihiro FURUZAWA,²⁷ Massimiliano GALEAZZI,²⁸ Luigi C. GALLO,²⁹
Poshak GANDHI,³⁰ Margherita GIUSTINI,² Andrea GOLDWURM,^{31,32} Liyi GU,²
Matteo GUAINAZZI,³³ Yoshito HABA,³⁴ Kouichi HAGINO,²⁰
Kenji HAMAGUCHI,^{7,35} Ilana M. HARRUS,^{7,35} Isamu HATSUKADE,³⁶
Katsuhiko HAYASHI,²⁰ Takayuki HAYASHI,³ Kiyoshi HAYASHIDA,³⁷
Junko S. HIRAGA,³⁸ Ann HORNSCHMEIER,⁷ Akio HOSHINO,³⁹
John P. HUGHES,⁴⁰ Yuto ICHINOHE,²³ Ryo IZUKA,²⁰ Hajime INOUE,⁴¹
Yoshiyuki INOUE,²⁰ Manabu ISHIDA,²⁰ Kumi ISHIKAWA,²⁰ Yoshitaka ISHISAKI,²³
Masachika IWAI,²⁰ Jelle KAASTRA,² Tim KALLMAN,⁷ Tsuneyoshi KAMAE,¹¹
Jun KATAOKA,⁴² Satoru KATSUDA,⁴³ Nobuyuki KAWAI,⁴⁴ Richard L. KELLEY,⁷
Caroline A. KILBOURNE,⁷ Takao KITAGUCHI,²⁶ Shunji KITAMOTO,³⁹
Tetsu KITAYAMA,⁴⁵ Takayoshi KOHMURA,⁴⁶ Motohide KOKUBUN,²⁰
Katsuji KOYAMA,⁴⁷ Shu KOYAMA,²⁰ Peter KRETSCHMAR,⁴⁸ Hans A. KRIMM,^{49,50}
Aya KUBOTA,⁵¹ Hideyo KUNIEDA,³ Philippe LAURENT,^{31,32} Shiu-Hang LEE,²⁰
Maurice A. LEUTENEGGER,⁷ Olivier O. LIMOUSIN,³² Michael LOEWENSTEIN,⁷
Knox S. LONG,⁵² David LUMB,³³ Greg MADEJSKI,⁴ Yoshitomo MAEDA,²⁰
Daniel MAIER,^{31,32} Kazuo MAKISHIMA,⁵³ Maxim MARKEVITCH,⁷
Hironori MATSUMOTO,³⁷ Kyoko MATSUSHITA,⁵⁴ Dan MCCAMMON,⁵⁵
Brian R. McNAMARA,⁵⁶ Missagh MEHDIPOUR,² Eric D. MILLER,¹³
Jon M. MILLER,⁵⁷ Shin MINESHIGE,²¹ Kazuhisa MITSUDA,²⁰
Ikuyuki MITSUISHI,³ Takuya MIYAZAWA,⁵⁸ Tsunefumi MIZUNO,²⁶
Hideyuki MORI,⁷ Koji MORI,³⁶ Koji MUKAI,^{7,35} Hiroshi MURAKAMI,⁵⁹
Richard F. MUSHOTZKY,⁶⁰ Takao NAKAGAWA,²⁰ Hiroshi NAKAJIMA,³⁷
Takeshi NAKAMORI,⁶¹ Shinya NAKASHIMA,⁵³ Kazuhiro NAKAZAWA,¹¹

Kumiko K. NOBUKAWA,⁶² Masayoshi NOBUKAWA,⁶³ Hirofumi NODA,^{64,65,†}
 Hirokazu ODAKA,⁴ Takaya OHASHI,²³ Masanori OHNO,²⁶ Takashi OKAJIMA,⁷
 Naomi OTA,⁶² Masanobu OZAKI,²⁰ Frits PAERELS,⁶⁶ Stéphane PALTANI,⁸
 Robert PETRE,⁷ Ciro PINTO,²⁴ Frederick S. PORTER,⁷ Katja POTTSCHMIDT,^{7,35}
 Christopher S. REYNOLDS,⁶⁰ Samar SAFI-HARB,⁶⁷ Shinya SAITO,³⁹
 Kazuhiro SAKAI,⁷ Toru SASAKI,⁵⁴ Goro SATO,²⁰ Kosuke SATO,⁵⁴ Rie SATO,²⁰
 Makoto SAWADA,⁶⁸ Norbert SCHARTEL,⁴⁸ Peter J. SERLEMITSOS,⁷
 Hiromi SETA,²³ Megumi SHIDATSU,⁵³ Aurora SIMIONESCU,²⁰
 Randall K. SMITH,¹⁴ Yang SOONG,⁷ Łukasz STAWARZ,⁶⁹
 Yasuharu SUGAWARA,²⁰ Satoshi SUGITA,⁴⁴ Andrew SZYMKOWIAK,¹⁷
 Hiroyasu TAJIMA,⁷⁰ Hiromitsu TAKAHASHI,²⁶ Tadayuki TAKAHASHI,²⁰
 Shin'ichiro TAKEDA,⁵⁸ Yoh TAKEI,²⁰ Toru TAMAGAWA,⁷¹ Takayuki TAMURA,²⁰
 Takaaki TANAKA,⁴⁷ Yasuo TANAKA,²⁰ Yasuyuki T. TANAKA,²⁶
 Makoto S. TASHIRO,⁷² Yuzuru TAWARA,³ Yukikatsu TERADA,⁷²
 Yuichi TERASHIMA,⁹ Francesco TOMBESI,^{7,60} Hiroshi TOMIDA,²⁰
 Yohko TSUBOI,⁴³ Masahiro TSUJIMOTO,²⁰ Hiroshi TSUNEMI,³⁷
 Takeshi Go TSURU,⁴⁷ Hiroyuki UCHIDA,⁴⁷ Hideki UCHIYAMA,⁷³
 Yasunobu UCHIYAMA,³⁹ Shutaro UEDA,²⁰ Yoshihiro UEDA,²¹
 Shin'ichiro UNO,⁷⁴ C. Megan URRY,¹⁷ Eugenio URSINO,²⁸ Shin WATANABE,²⁰
 Norbert WERNER,^{75,76,26} Dan R. WILKINS,⁴ Brian J. WILLIAMS,⁵²
 Shinya YAMADA,²³ Hiroya YAMAGUCHI,⁷ Kazutaka YAMAOKA,³
 Noriko Y. YAMASAKI,²⁰ Makoto YAMAUCHI,³⁶ Shigeo YAMAUCHI,⁶²
 Tahir YAQOOB,^{7,35} Yoichi YATSU,⁴⁴ Daisuke YONETOKU,²⁵ Irina ZHURAVLEVA,^{4,5}
 Abderahmen ZOGHBI,⁵⁷ and Taiki KAWAMURO⁷⁷

¹Dublin Institute for Advanced Studies, 31 Fitzwilliam Place, Dublin 2, Ireland

²SRON Netherlands Institute for Space Research, Sorbonnelaan 2, 3584 CA Utrecht, The Netherlands

³Department of Physics, Nagoya University, Furo-cho, Chikusa-ku, Nagoya, Aichi 464-8602, Japan

⁴Kavli Institute for Particle Astrophysics and Cosmology, Stanford University, 452 Lomita Mall, Stanford, CA 94305, USA

⁵Department of Physics, Stanford University, 382 Via Pueblo Mall, Stanford, CA 94305, USA

⁶SLAC National Accelerator Laboratory, 2575 Sand Hill Road, Menlo Park, CA 94025, USA

⁷NASA, Goddard Space Flight Center, 8800 Greenbelt Road, Greenbelt, MD 20771, USA

⁸Department of Astronomy, University of Geneva, ch. d'Écogia 16, CH-1290 Versoix, Switzerland

⁹Department of Physics, Ehime University, 2-5 Bunkyo-cho, Matsuyama, Ehime 790-8577, Japan

¹⁰Department of Physics and Oskar Klein Center, Stockholm University, 106 91 Stockholm, Sweden

¹¹Department of Physics, The University of Tokyo, 7-3-1 Hongo, Bunkyo-ku, Tokyo 113-0033, Japan

¹²Research Center for the Early Universe, School of Science, The University of Tokyo, 7-3-1 Hongo, Bunkyo-ku, Tokyo 113-0033, Japan

¹³Kavli Institute for Astrophysics and Space Research, Massachusetts Institute of Technology, 77 Massachusetts Avenue, Cambridge, MA 02139, USA

¹⁴Harvard-Smithsonian Center for Astrophysics, 60 Garden Street, Cambridge, MA 02138, USA

¹⁵Lawrence Livermore National Laboratory, 7000 East Avenue, Livermore, CA 94550, USA

¹⁶Department of Physics and Astronomy, Wayne State University, 666 W. Hancock St, Detroit, MI 48201, USA

¹⁷Department of Physics, Yale University, New Haven, CT 06520-8120, USA

¹⁸Department of Astronomy, Yale University, New Haven, CT 06520-8101, USA

- ¹⁹Centre for Extragalactic Astronomy, Department of Physics, University of Durham, South Road, Durham, DH1 3LE, UK
- ²⁰Japan Aerospace Exploration Agency, Institute of Space and Astronautical Science, 3-1-1 Yoshino-dai, Chuo-ku, Sagami-hara, Kanagawa 252-5210, Japan
- ²¹Department of Astronomy, Kyoto University, Kitashirakawa-Oiwake-cho, Sakyo-ku, Kyoto, Kyoto 606-8502, Japan
- ²²The Hakubi Center for Advanced Research, Kyoto University, Yoshida-honmachi, Sakyo-ku, Kyoto 606-8501, Japan
- ²³Department of Physics, Tokyo Metropolitan University, 1-1 Minami-Osawa, Hachioji, Tokyo 192-0397, Japan
- ²⁴Institute of Astronomy, University of Cambridge, Madingley Road, Cambridge, CB3 0HA, UK
- ²⁵Faculty of Mathematics and Physics, Kanazawa University, Kakuma-machi, Kanazawa, Ishikawa 920-1192, Japan
- ²⁶School of Science, Hiroshima University, 1-3-1 Kagamiyama, Higashi-Hiroshima, Hiroshima 739-8526, Japan
- ²⁷Fujita Health University, 1-98 Dengakugakubo, Kutsukake-cho, Toyoake, Toyoake, Aichi 470-1192, Japan
- ²⁸Physics Department, University of Miami, 1320 Campo Sano Dr., Coral Gables, FL 33146, USA
- ²⁹Department of Astronomy and Physics, Saint Mary's University, 923 Robie Street, Halifax, NS, B3H 3C3, Canada
- ³⁰Department of Physics and Astronomy, University of Southampton, Highfield, Southampton, SO17 1BJ, UK
- ³¹Laboratoire APC, 10 rue Alice Domon et Léonie Duquet, 75013 Paris, France
- ³²CEA Saclay, 91191 Gif sur Yvette, France
- ³³European Space Research and Technology Center, Keplerlaan 1, 2201 AZ Noordwijk, The Netherlands
- ³⁴Department of Physics and Astronomy, Aichi University of Education, 1 Hirosawa, Igaya-cho, Kariya, Aichi 448-8543, Japan
- ³⁵Department of Physics, University of Maryland Baltimore County, 1000 Hilltop Circle, Baltimore, MD 21250, USA
- ³⁶Department of Applied Physics and Electronic Engineering, University of Miyazaki, 1-1 Gakuen Kibanadai-Nishi, Miyazaki, Miyazaki 889-2192, Japan
- ³⁷Department of Earth and Space Science, Osaka University, 1-1 Machikaneyama-cho, Toyonaka, Osaka 560-0043, Japan
- ³⁸Department of Physics, Kwansei Gakuin University, 2-1 Gakuen, Sanda, Hyogo 669-1337, Japan
- ³⁹Department of Physics, Rikkyo University, 3-34-1 Nishi-Ikebukuro, Toshima-ku, Tokyo 171-8501, Japan
- ⁴⁰Department of Physics and Astronomy, Rutgers University, 136 Frelinghuysen Road, Piscataway, NJ 08854, USA
- ⁴¹Meisei University, 2-1-1 Hodokubo, Hino, Tokyo 191-8506, Japan
- ⁴²Research Institute for Science and Engineering, Waseda University, 3-4-1 Ohkubo, Shinjuku-ku, Tokyo 169-8555, Japan
- ⁴³Department of Physics, Chuo University, 1-13-27 Kasuga, Bunkyo-ku, Tokyo 112-8551, Japan
- ⁴⁴Department of Physics, Tokyo Institute of Technology, 2-12-1 Ookayama, Meguro-ku, Tokyo 152-8550, Japan
- ⁴⁵Department of Physics, Toho University, 2-2-1 Miyama, Funabashi, Chiba 274-8510, Japan
- ⁴⁶Department of Physics, Tokyo University of Science, 2641 Yamazaki, Noda, Chiba 278-8510, Japan
- ⁴⁷Department of Physics, Kyoto University, Kitashirakawa-Oiwake-cho, Sakyo, Kyoto, Kyoto 606-8502, Japan
- ⁴⁸European Space Astronomy Center, Camino Bajo del Castillo, s/n., 28692 Villanueva de la Cañada, Madrid, Spain
- ⁴⁹Universities Space Research Association, 7178 Columbia Gateway Drive, Columbia, MD 21046, USA
- ⁵⁰National Science Foundation, 4201 Wilson Blvd, Arlington, VA 22230, USA

- ⁵¹Department of Electronic Information Systems, Shibaura Institute of Technology, 307 Fukasaku, Minuma-ku, Saitama, Saitama 337-8570, Japan
- ⁵²Space Telescope Science Institute, 3700 San Martin Drive, Baltimore, MD 21218, USA
- ⁵³Institute of Physical and Chemical Research, 2-1 Hirosawa, Wako, Saitama 351-0198, Japan
- ⁵⁴Department of Physics, Tokyo University of Science, 1-3 Kagurazaka, Shinjuku-ku, Tokyo 162-8601, Japan
- ⁵⁵Department of Physics, University of Wisconsin, Madison, WI 53706, USA
- ⁵⁶Department of Physics and Astronomy, University of Waterloo, 200 University Avenue West, Waterloo, Ontario, N2L 3G1, Canada
- ⁵⁷Department of Astronomy, University of Michigan, 1085 South University Avenue, Ann Arbor, MI 48109, USA
- ⁵⁸Okinawa Institute of Science and Technology Graduate University, 1919-1 Tancha, Onna-son, Kunigami-gun, Okinawa 904-0495, Japan
- ⁵⁹Faculty of Liberal Arts, Tohoku Gakuin University, 2-1-1 Tenjinzawa, Izumi-ku, Sendai, Miyagi 981-3193, Japan
- ⁶⁰Department of Astronomy, University of Maryland, College Park, MD 20742, USA
- ⁶¹Faculty of Science, Yamagata University, 1-4-12 Kojirakawa-machi, Yamagata, Yamagata 990-8560, Japan
- ⁶²Department of Physics, Nara Women's University, Kita-uoyanishi-machi, Nara, Nara 630-8506, Japan
- ⁶³Department of Teacher Training and School Education, Nara University of Education, Takabatake-cho, Nara, Nara 630-8528, Japan
- ⁶⁴Frontier Research Institute for Interdisciplinary Sciences, Tohoku University, 6-3 Aramaki-zaaoba, Aoba-ku, Sendai, Miyagi 980-8578, Japan
- ⁶⁵Astronomical Institute, Tohoku University, 6-3 Aramaki-zaaoba, Aoba-ku, Sendai, Miyagi 980-8578, Japan
- ⁶⁶Astrophysics Laboratory, Columbia University, 550 West 120th Street, New York, NY 10027, USA
- ⁶⁷Department of Physics and Astronomy, University of Manitoba, Winnipeg, MB R3T 2N2, Canada
- ⁶⁸Department of Physics and Mathematics, Aoyama Gakuin University, 5-10-1 Fuchinobe, Chuo-ku, Sagami-hara, Kanagawa 252-5258, Japan
- ⁶⁹Astronomical Observatory of Jagiellonian University, ul. Orla 171, 30-244 Kraków, Poland
- ⁷⁰Institute for Space-Earth Environmental Research, Nagoya University, Furo-cho, Chikusa-ku, Aichi 464-8601, Japan
- ⁷¹RIKEN Nishina Center, 2-1 Hirosawa, Wako, Saitama 351-0198, Japan
- ⁷²Department of Physics, Saitama University, 255 Shimo-Okubo, Sakura-ku, Saitama, 338-8570, Japan
- ⁷³Faculty of Education, Shizuoka University, 836 Ohya, Suruga-ku, Shizuoka 422-8529, Japan
- ⁷⁴Faculty of Health Sciences, Nihon Fukushi University, 26-2 Higashi Haemi-cho, Handa, Aichi 475-0012, Japan
- ⁷⁵MTA-Eötvös University Lendület Hot Universe Research Group, Pázmány Péter sétány 1/A, Budapest, 1117, Hungary
- ⁷⁶Department of Theoretical Physics and Astrophysics, Faculty of Science, Masaryk University, Kotlářská 2, Brno, 602 00, Czech Republic
- ⁷⁷National Astronomical Observatory of Japan, 2-21-1 Osawa, Mitaka, Tokyo 181-8588, Japan

*The corresponding authors are Hirofumi Noda, Yasushi Fukazawa, Frederick S. Porter, Laura W. Brenneman, Koichi Hagino, Taiki Kawamuro, Shinya Nakashima, Christopher S. Reynolds, and Takaaki Tanaka.

†E-mail: hirofumi.noda@astr.tohoku.ac.jp

Received 2017 September 7; Accepted 2017 November 16

Abstract

The origin of the narrow Fe-K α fluorescence line at 6.4 keV from active galactic nuclei has long been under debate; some of the possible sites are the outer accretion disk, the broad line region, a molecular torus, or interstellar/intracluster media. In 2016 February–March, we performed the first X-ray microcalorimeter spectroscopy with the Soft

X-ray Spectrometer (SXS) on board the Hitomi satellite of the Fanaroff–Riley type I radio galaxy NGC 1275 at the center of the Perseus cluster of galaxies. With the high-energy resolution of ~ 5 eV at 6 keV achieved by Hitomi/SXS, we detected the Fe-K α line with $\sim 5.4\sigma$ significance. The velocity width is constrained to be 500–1600 km s $^{-1}$ (FWHM for Gaussian models) at 90% confidence. The SXS also constrains the continuum level from the NGC 1275 nucleus up to ~ 20 keV, giving an equivalent width of ~ 20 eV for the 6.4 keV line. Because the velocity width is narrower than that of the broad H α line of ~ 2750 km s $^{-1}$, we can exclude a large contribution to the line flux from the accretion disk and the broad line region. Furthermore, we performed pixel map analyses on the Hitomi/SXS data and image analyses on the Chandra archival data, and revealed that the Fe-K α line comes from a region within ~ 1.6 kpc of the NGC 1275 core, where an active galactic nucleus emission dominates, rather than that from intracluster media. Therefore, we suggest that the source of the Fe-K α line from NGC 1275 is likely a low-covering-fraction molecular torus or a rotating molecular disk which probably extends from a parsec to hundreds of parsecs scale in the active galactic nucleus system.

Key words: galaxies: active — galaxies: individual (NGC 1275) — galaxies: radio galaxy — methods: observational — X-rays: galaxies

1 Introduction

Fluorescent Fe-K α emission is the most ubiquitous atomic feature in the X-ray spectrum of non-blazar-type active galactic nuclei (AGN; e.g., Pounds et al. 1990; Nandra & Pounds 1994). The line is produced by the irradiation of low- and intermediate-ionization circumnuclear gas by the hard X-ray continuum emitted from the corona of the accreting supermassive black hole (SMBH). Thus, it provides a powerful probe of the circumnuclear environment of an AGN.

There are at least three observable Fe-K emission components. Irradiation of the inner accretion disk gives a relativistically broadened line (Fabian et al. 1989; Tanaka et al. 1995) that can be used to constrain the inclination of the inner disk and the black hole spin (Iwasawa et al. 1996; Brenneman et al. 2011). The much more distant interstellar medium and disk winds can be photo-ionized and produce narrow ionized (Fe XXV and Fe XXVI) iron lines (Yaqoob et al. 2003). Finally, most AGN display a relatively narrow (< 3000 km s $^{-1}$) and neutral Fe-K α line at 6.4 keV. The origin of this line is unclear, with candidates being the outer edge of the accretion disk, the broad line region (BLR), the dusty torus of unified AGN schemes (Antonucci 1993; Urry & Padovani 1995), or the larger-scale reservoir from which the AGN is fueled.

To date, most studies of the narrow Fe-K α line have focused on X-ray-bright Seyfert galaxies utilizing both dispersive high-resolution spectrometers such as the Chandra/High-Energy Transmission Grating (HETG; Canizares et al. 2000) and non-dispersive moderate-resolution spectrometers such as Chandra/Advanced CCD Imaging Spectrometer (ACIS; Garmire et al. 2003) and

XMM-Newton/European Photon Imaging Camera (EPIC; Turner et al. 2001; Strüder et al. 2001). Using HEG data, Shu, Yaqoob, and Wang (2010, 2011) reported that the narrow Fe-K α line from typical Seyfert galaxies exhibits velocity widths greater than ~ 2000 km s $^{-1}$ (FWHM). Subsequently, Gandhi, Hönig, and Kishimoto (2015) and Minezaki and Matsushita (2015) compared object-by-object velocity widths of the Fe-K α line, the broad Balmer lines of hydrogen, and those corresponding to dust sublimation radii, and found that the Fe-K α source lies between the BLR and dust sublimation radius. In contrast, the origin of the Fe-K α line from radio-loud or low-luminosity AGN remains unclear in spite of observations with these high-performance X-ray spectrometers, principally due to their relatively low equivalent widths and fluxes (see Fukazawa et al. 2011). We need the leap in sensitivity and resolution provided by the Soft X-ray Spectrometer (SXS; Kelley et al. 2016) on board the Hitomi satellite (Takahashi et al. 2016) to establish a picture for the circumnuclear distribution of gas in AGN via studies of the Fe-K α line.

In this paper, we focus on the X-ray properties of the radio-loud AGN NGC 1275 which resides at the center of the Perseus cluster of galaxies ($z_* = 0.017284$; Hitomi Collaboration 2018a). Chandra and XMM-Newton observations reveal signatures of interaction between the jets from NGC 1275 and the cool core of the intracluster medium (ICM), most notably the presence of kpc-scale cavities and weak shocks or sound waves in the ICM (e.g., Fabian et al. 2006). There is compelling evidence that these jet–ICM interactions in cool-core galaxy clusters heat the ICM, preventing the ICM core from undergoing a cooling catastrophe. Being the brightest example, the Perseus cluster and

NGC 1275 have thus been recognized as one of the most important targets for gaining an understanding of the feedback loop that allows a central AGN to regulate a cluster core (e.g., McNamara & Nulsen 2007). For this reason, the core of the Perseus cluster was the first science target for the SXS on board Hitomi. This X-ray microcalorimeter observation produced a spectrum of the ICM with unprecedented spectral resolution, finding a surprisingly quiescent turbulent velocity of $\sim 160 \text{ km s}^{-1}$ despite the vigorous AGN feedback (Hitomi Collaboration 2016). This same observation gives us our first view of an AGN, NGC 1275, with an X-ray microcalorimeter—that is the focus of this paper.

The X-ray properties of NGC 1275 have been studied for many years. Fabian et al. (2015) compiled a 40 yr X-ray light curve from archival and historical multi-mission data, and compared it to the 90 GHz flux over the same time. They found that the X-ray and radio flux were correlated. They also found that the source was very bright in the 1970s–1980s, fading to a minimum in 2000–2005, and has been slowly brightening since that time. The X-ray spectrum observed by XMM-Newton in 2001 exhibited the presence of a clear narrow Fe-K α line with an equivalent width (EW) of $\sim 165 \text{ eV}$ relative to the AGN continuum (Churazov et al. 2003). A later XMM-Newton observation in 2006 found that the EW had decreased to 70–80 eV (Yamazaki et al. 2013), mostly due to an increase in the AGN continuum flux, while the line flux was roughly constant. However, the line width has never been successfully measured, and hence it was not known which region mainly generates the Fe-K α emission in NGC 1275. Here we report the first measurements of the Fe-K α line width in NGC 1275, providing such a measurement from a radio-loud, central cluster AGN. This is the first X-ray spectroscopy of an AGN with an X-ray microcalorimeter.

NGC 1275 harbors a SMBH with a mass of $M_{\text{BH}} \sim 3.4 \times 10^8 M_{\odot}$ (Wilman et al. 2005) or $\sim 8 \times 10^8 M_{\odot}$ (Scharwächter et al. 2013), and exhibits a relatively low Eddington ratio, $L_B/L_{\text{Edd}} \sim 3 \times 10^{-4}$ (e.g., Sikora et al. 2007). The AGN has often been classified as a Fanaroff–Riley type-I (FR I) radio galaxy (Laing et al. 1983), but it is still unclear whether or not this system has a Seyfert-like BLR. While a broad H α line with velocity width of $\sim 2750 \text{ km s}^{-1}$ (FWHM) was observed during the bright phase in 1984 (Ho et al. 1997), no optical broad lines were detected by HST when the source was in the faint phase in 2000 (Balmaverde & Capetti 2014). In the infrared band, Scharwächter et al. (2013) reported [Fe II], H $_2$, He I, and Br γ lines with velocity widths of ~ 380 – 1000 km s^{-1} (FWHM) from a resolved rotating molecular disk which has a size of a few hundreds of parsecs.

In the present paper, we analyze not only the Fe-K α line emission from NGC 1275 but also the broad-band

continuum from this AGN. The continuum studies are enabled by fact that the SXS (at the focal point of one of the Hitomi Soft X-ray Telescopes; SXT) has sensitivity up to $\sim 20 \text{ keV}$, an energy at which the AGN dominates over the ICM emission, and a very low background. In section 2, we briefly describe the Hitomi observation and data reduction as well as the data from other satellites that we shall use in this investigation. Our analyses and results are reported in section 3, focusing first on the nature of the Fe-K α line (subsection 3.1) and then on the broad-band AGN emission (subsection 3.2). We discuss the astrophysical implications in section 4, developing the case that the Fe-K α line originates from the torus or the molecular disk seen by Scharwächter et al. (2013). Unless otherwise stated, the tables and figures use 90% and 1σ error ranges. All abundances are quoted relative to the Lodders and Palme (2009) solar abundance set. Photoelectric cross-sections for the absorption model are obtained from Bałucińska-Church and McCammon (1992).

2 Observation and data reduction

2.1 Hitomi

The Hitomi observations of the core of the Perseus cluster and NGC 1275 were performed on 2016 February 24–27 and March 4–7 with three different nominal pointing positions. Here, we utilize the SXS data obtained on February 25–27 and March 4–6 (OBSID 100040020–100040050) which were derived at the same nominal position with a total on-source exposure of approximately 240 ks. The SXS successfully achieved an unprecedented in-orbit energy resolution of $\sim 4.9 \text{ eV}$ at 6 keV in 35 calorimeter pixels which covered a field of view (FOV) of $\sim 3' \times 3'$ (Porter et al. 2016; Leutenegger et al. 2016). The SXT focuses X-rays onto the SXS with a half power diameter (HPD) of 1.2 (Okajima et al. 2016). The in-orbit energy resolution and the HPD were better than the formal requirements of 7 eV and 1.7 (Takahashi et al. 2016), respectively. Although energies below $\sim 2 \text{ keV}$ could not be observed by the SXS due to the closed gate valve on the cryostat (Eckart et al. 2016), the extension of its bandpass up to $\sim 20 \text{ keV}$, which was also much beyond the requirement of 12 keV (Takahashi et al. 2016), proves extremely useful for this investigation of NGC 1275. The Soft X-ray Imager (SXI: Tsunemi et al. 2016), the Hard X-ray Imager (HXI: Nakazawa et al. 2016), and the Soft Gamma-ray Detector (SGD: Watanabe et al. 2016) were inactive during the observations of the Perseus cluster used in the present paper.

The SXS cleaned datasets were reduced via the pipeline version 03.01.006.007 (Angelini et al. 2016). In order to utilize the energy range above 16 keV, we apply `sxsextend` in HEASoft-6.20 to the cleaned datasets, and extract events

Table 1. List of the archival data of XMM-Newton and Chandra.

OBSID	Observation date	Exposure (ks)	Angular offset (')	Source / BGD extraction regions
XMM-Newton/PN and MOS				
0085110101	2001 January 30	60*	0.001	14'' circle / 60''–63'' annulus
0305780101	2006 January 29	141*	0.038	
Chandra/HEG				
333	1999 October 10	27	0.011	4'' circle / None
428	2000 August 25	25	0.011	
Chandra/ACIS				
6139	2004 October 4	56	0.007	4''–45'' annulus / off-source 50'' circle
4946	2004 October 6	24	0.007	
4948	2004 October 9	119	0.007	
4947	2004 October 11	30	0.007	
4949	2004 October 12	29	0.007	
4950	2004 October 12	97	0.007	
4952	2004 October 14	164	0.007	
4951	2004 October 17	96	0.007	
4953	2004 October 18	30	0.007	
6145	2004 October 19	85	0.007	
6146	2004 October 20	47	0.007	

*The integrated total exposure for all the detectors, PN and MOS.

with the screenings which use the relation between energy and rise time of every X-ray event, and with the removals of frame events using time coincidence among pixels. Moreover, we select events with high primary grade to use the highest-resolution events. Spectra are extracted via `xselect`. After these reductions, we further apply two types of gain corrections: one is the “ z correction” and the other is the “parabolic correction.” The z correction is a linear gain correction to all the pixels in order to align the central energy of the 6.7004 keV Fe XXV He α emission line seen in the emission from the hot gas in the Perseus cluster to the redshift of NGC 1275 of 0.017284. The parabolic correction is applied to align the central energies of emission lines in the 1.8–9.0 keV band, with the function $\Delta E_{\text{corr}} = A(E_{\text{obs}} - E_{\text{res}})^2 + B(E_{\text{obs}} - E_{\text{res}})$, where E_{obs} and E_{res} are the observed energy and the redshifted Fe XXV He α energy, respectively. The two gain corrections are the same as those used in Hitomi Collaboration (2018c), and are of the order of 1 eV (see the appendix in Hitomi Collaboration 2018c for further details). In the present paper, we use the datasets after both z correction and parabolic correction are applied, unless otherwise stated.

In spectral analyses, the non-X-ray background (NXB: Kilbourne et al. 2016) events are modeled by `sxsnxbgen` in `ftools`. The redistribution matrix file (RMF) is prepared by `sxsmkrmf` in HEAsoft-6.20 as an extra-large matrix which can include the escape peak and electron loss continuum effects. The ancillary response files (ARFs) are prepared via `aharfgen` in HEAsoft-6.20. The ARF for a point-like source is created, assuming a point-like source at $(\alpha_{\text{J2000.0}}, \delta_{\text{J2000.0}})$

$= (3^{\text{h}}19^{\text{m}}48^{\text{s}}.16, 41^{\circ}30'42''.10)$. The ARF for a diffuse source is created using as input a sky image from Chandra in the 1.8–9.0 keV band where the AGN region within 10'' from NGC 1275 is replaced with the average adjacent brightness.

2.2 Other X-ray satellites: XMM-Newton and Chandra

To discuss the spatial extent of the Fe-K α line source (sub-subsection 3.1.3), we utilize archival datasets taken with XMM-Newton and Chandra, complementary to the Hitomi data. The XMM-Newton and Chandra data are reprocessed using the SAS-16.0.0 and CIAO-4.8 software, respectively.

XMM-Newton observations with nominal positions very close to NGC 1275 were conducted in 2001 January and 2006. We use the two long datasets (>60 ks) with the EPIC MOS and PN detectors (see table 1). Exploiting the moderate angular resolution of $\sim 15''$ (HPD), we analyze the AGN spectra.

Chandra has been intensively used to study the Perseus cluster, resulting in 31 publicly available archival datasets as of 2016. The unprecedented angular resolution ($\lesssim 1''$) enables us to precisely localize the Fe-K α line by discriminating between the AGN and emission from the cluster gas. We utilize all the datasets of the HETG read out onto the ACIS. The dispersed High-Energy Grating (HEG) data are analyzed, whereas the dispersed Medium-Energy Grating (MEG) data are not used because it does not cover the

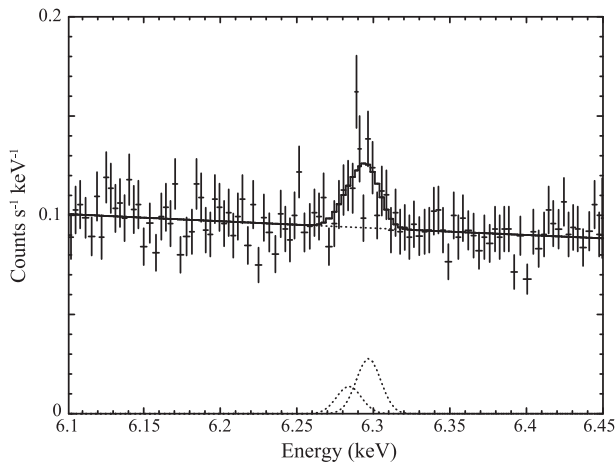


Fig. 1. The 6.1–6.45 keV SXS spectrum including the neutral Fe-K α line at ~ 6.4 keV in the rest frame. It is fitted with the model of `powerlaw + zgauss1 + zgauss2`, which corresponds to a sum of spectral continua from the ICM and AGN, an Fe-K α_1 , and an Fe-K α_2 emission line, respectively. (Color online)

Fe-K α line energy. The other Chandra datasets were taken with ACIS in the imaging mode. Although pile-up is significant in the central region ($<4''$; see the detail in subsubsection 3.1.3), the possible Fe-K α line flux in the outer region ($>4''$) can be constrained. We select (1) the data sets which have an angular offset from NGC 1275 less than 0.1 in order to make use of high angular resolution (0.5), and (2) those taken in 2004 to reduce systematic uncertainties associated with the aging of the instruments. The final datasets we use are summarized in table 1.

3 Data analysis and results

3.1 Fe-K α spectral and spatial analyses

We begin by examining the spectral and spatial structure of the neutral Fe-K α line emission.

3.1.1 The SXS spectrum

We analyze a spectrum extracted from a field of 3×3 pixels (pixel #0–#8) of the microcalorimeter array centered on NGC 1275 (which is in pixel #4), since $\sim 95\%$ of the AGN counts are contained in this region (Hitomi Collaboration 2016). Figure 1 shows this nine-pixel NXB-subtracted spectrum in the 6.1–6.45 keV (observed) range; a clear emission line can be seen at ~ 6.28 keV, which corresponds to ~ 6.40 keV in the rest frame. Detailed spectral fitting at microcalorimeter resolution must account for the fact that the neutral Fe-K α line is actually a doublet with intrinsic energies 6.404 keV and 6.391 keV for Fe-K α_1 and Fe-K α_2 , respectively. We fit this section of the spectrum with a model consisting of a power law (representing the sum of the ICM and AGN continuum) and two redshifted Gaussian lines with intrinsic energies of Fe-K α_1 and Fe-K α_2 (XSPEC

model `powerlaw + zgauss1 + zgauss2`). Atomic physics dictates that the intrinsic intensity of Fe-K α_1 is twice of that of Fe-K α_2 , and so the relative normalization of the Gaussian lines are linked accordingly. Free parameters of the model are the photon index Γ and the normalization N_{PL} of `powerlaw`, the redshift z and overall intensity of the Fe-K α_1 /Fe-K α_2 doublet, and the (common) velocity width σ of the Fe-K α_1 /Fe-K α_2 doublet. Fitting is performed using microcalorimeter energy bins of 1 eV; we do not further bin the spectrum. We perform the spectral fitting with C-statistics (Cash 1979), because of the modest count rate in each bin.

This simple model provides a good description of the spectrum (with C-statistics/d.o.f. = 326.2/344).¹ The best-fitting parameter values are summarized in table 2. Despite the fact that the sum of the EWs of the two Fe-K α lines ($\text{EW}_1 + \text{EW}_2$) is just ~ 9 eV, they are detected with a high significance level of $\sim 5.4\sigma$ thanks to the high energy resolution of the SXS. This clearly illustrates the line detecting capability of X-ray microcalorimeters. After including the effects of the instrumental broadening in the modeling, the Fe-K α lines have a resolved velocity width with the Gaussian sigma of 4.4–13.1 eV (90% confidence range), corresponding to a velocity width of 500–1500 km s $^{-1}$ (FWHM; 90% confidence range). A Gaussian model is a good fit to the data.

Figure 2 shows the confidence contours between the Fe-K α intensity (sum of two lines) and redshift. The redshift of $0.01702^{+0.00059}_{-0.00060}$ is consistent, within 90% errors, with the value ($z_* = 0.017284$) measured by optical emission lines of stars in NGC 1275 (Hitomi Collaboration 2018a). This shows that the center energies of the Hitomi detected lines are consistent with the neutral values of Fe-K α_1 and Fe-K α_2 lines at 6.404 and 6.391 keV, respectively, at the redshift of NGC 1275. However, the derived AGN redshift is inconsistent with that of the ambient ICM emission ($z_{\text{ICM}} = 0.01767 \pm 0.00003$; Hitomi Collaboration 2016). Refer to Hitomi Collaboration (2018a) for more discussions about the redshift difference between NGC 1275 and ICM.

In order to consider systematic errors which come from the SXS gain uncertainty and the spatial distribution of the ICM bulk motion, we next fit the 6.1–6.45 keV spectrum extracted from the event sets with neither the z nor parabolic correction, with the same models and parameter settings as above. As shown in table 2, the Gaussian sigma becomes 5.2–14.4 eV (90% confidence range after including the instrumental broadening in the modeling), which corresponds to the 90% confidence range of the velocity width of 600–1600 km s $^{-1}$ (FWHM). The line detection significance

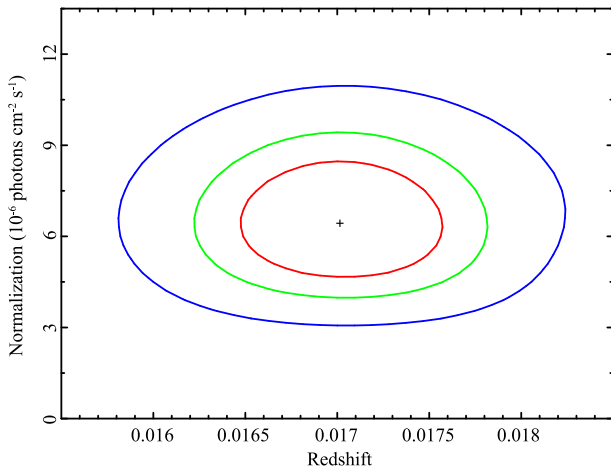
¹ C-statistics is distributed as χ^2 in the case of a large number of samples (Cash 1979).

Table 2. Results of the fit to the 6.1–6.45 keV spectrum of the SXS nine on-core pixels, with and without the z and parabolic corrections.

Component	Parameter	With z & parabolic corr.	Without z & parabolic corr.
powerlaw	Γ	$2.49^{+0.86}_{-1.22}$	$2.55^{+0.86}_{-1.17}$
	N_{PL}^*	$0.07^{+0.45}_{-0.06}$	$0.08^{+0.55}_{-0.07}$
zgauss1	E_1 (keV)	6.404 (fix)	
	σ_1 (eV)	$7.79^{+5.35}_{-3.37}$	$8.93^{+5.49}_{-3.73}$
	z_1	$0.01702^{+0.00059}_{-0.00060}$	$0.01733^{+0.00065}_{-0.00064}$
	N_1^\dagger	$4.30^{+1.48}_{-1.29}$	$4.48^{+1.53}_{-1.34}$
	E_2 (keV)	6.391 (fix)	
zgauss2	σ_2 (eV)	$=\sigma_1$	
	z_2	$=z_1$	
	N_2^\dagger	$=0.5 \times N_1$	
	$\text{EW}_1 + \text{EW}_2$ (eV)	$8.9^{+3.1}_{-2.7}$	$9.2^{+3.2}_{-2.8}$
	C-statistics/d.o.f.	326.2/344	325.5/344

*The powerlaw normalization at 1 keV, in units of photons $\text{keV}^{-1} \text{cm}^{-2} \text{s}^{-1}$.

†The zgauss normalization, in units of 10^{-6} photons $\text{cm}^{-2} \text{s}^{-1}$.

**Fig. 2.** Contours of confidence level of 68% (red), 90% (green), and 99% (blue) between the normalization ($K_{\alpha 1} + K_{\alpha 2}$) and redshift in the Fe-K α line region fitting. (Color online)

is still $\sim 5.4\sigma$. The systematic increase of the line width is ~ 1 eV, and this is consistent with that due to the gain uncertainty of the SXS and/or the region-by-region ICM bulk motion (Hitomi Collaboration 2018a). The redshift becomes $0.01733^{+0.00065}_{-0.00064}$, which is consistent, within statistical 90% error, with that derived from the spectrum with the gain corrections, and with the optically measured value ($z_* = 0.017284$). Thus, even when the systematic errors are taken into account, the central energies of the Fe-K α lines are consistent with their neutral values. Hereafter, we thus utilize the velocity width range of ~ 500 – 1600 km s^{-1} (FWHM), taking into account the systematic uncertainties.

3.1.2 Spatial distribution from SXS data

The Perseus cluster possesses a system of atomic and molecular filaments that extend throughout the inner core of the cluster (see the detail in subsection 4.1). The origin of this cold gas, which is embedded within the hot ICM, is still debated; it may be condensing via thermal instability from the hot ICM, or it may be cold gas from the galaxy that is uplifted into the ICM by AGN activity. Either way, as discussed more extensively below, irradiation of this cold gas by the hot ICM and the central AGN can produce spatially extended Fe-K α fluorescence. We begin our exploration (and ultimate rejection) of this possibility for the observed Fe-K α fluorescence by using the imaging capability of the SXS to directly examine the spatial distribution of the Fe-K α emission.

We start by extracting spectra from individual pixels of the SXS microcalorimeter array. To select time intervals when the satellite pointing was stable, we use the good time interval (GTI) with the condition of a first Euler angle of $49^\circ 93' - 49^\circ 9325$ and second angle of $48^\circ 4812' - 48^\circ 4826$. We use the same RMF and ARF as those utilized in subsubsection 3.1.1 (see subsection 2.1). The individual pixel spectra are then fitted with the same model employed above, except that σ_1 and σ_2 are fixed at 7.79 eV, which is same as that in table 2. As a result, we can derive a pixel distribution of the count rate of the Fe-K α line photons as shown on the left of figure 3. It includes 1σ uncertainties of 6×10^{-7} and $(2-3) \times 10^{-7} \text{ photons cm}^{-2} \text{s}^{-1}$ in the peak position (Pixel 4) and in the faint end (Pixels 9, 11, 19, 21, 23, 24, 26, 30, 32, and 34). We find that the Fe-K α count rate in the on-core

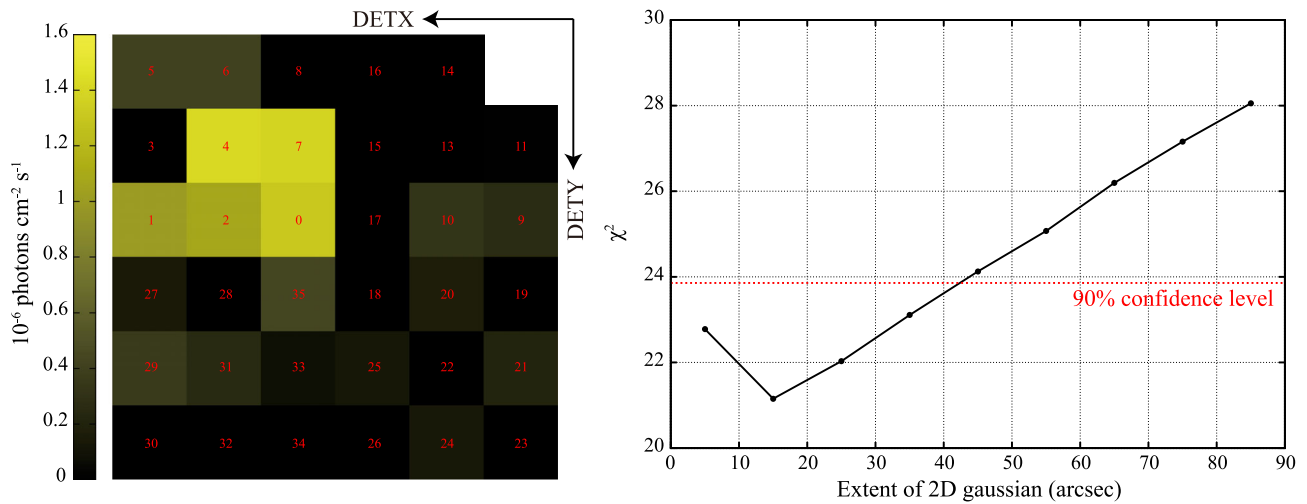


Fig. 3. Left: SXS pixel distribution of the Fe-K α count rate. Right: Plot of extent of source versus χ^2 values when the extent of the simulated 2D Gaussian source, which is fitted to the Fe-K α map (left panel), is changed as 5'', 15'', ..., 85''.

pixel is highest, as expected, and those in the surrounding eight pixels are higher than off-AGN regions, consistent with the Hitomi PSF, as detailed below.

Using this observed distribution of the count rate of Fe-K α photons, we constrain the source extent by comparing with model distributions blurred by the two-dimensional SXT point spread function (PSF) as computed using the `simx` v2.4.1 package. We use the PSF two-dimensional data file² taken by the beam-line experiment of the flight SXT-S at ISAS/JAXA in 2014. First, data from the Hitomi star trackers are used to determine the precise location of NGC 1275 on the SXS array, which we determine to be (DETX, DETY) = (4.85, 2.21). Next, we simulate the SXS image of a point source of 6.4 keV line photons, producing a grid of models with different source locations. We produce an 11 × 11 grid of DETX and DETY with a step size of 0.2 pixels. Comparing these models to the observed Fe-K α count rate map using the χ^2 statistic and making a confidence contour of DETX vs. DETY, we confirm that the best-fit location of the Fe-K α source becomes (DETX, DETY) = (4.7 ± 0.4, 2.5 ± 0.4), consistent with the position of NGC 1275.

Finally, we simulate a source that has an extended Gaussian profile, centered on NGC 1275, with $\sigma = 5'', 15'', 25'', \dots, 85''$. The angular resolution of the SXS + SXT is not enough, and the ratios between the Fe-K α and continuum count rates in the SXS pixel map are too low to limit complex source emission models which have effective extents smaller than the PSF. Hence, we choose a Gaussian as a simple model which can fit the data and constrain the source extent, considering a relatively smeared structure better than peakier models. The change in the χ^2 statistic

as a function of extent is shown on the right of figure 3. Thus, the Hitomi SXS data show that the Fe-K α source is constrained to have an extent of less than $\sim 42''$ or ~ 17 kpc at the distance of NGC 1275.

3.1.3 Fe-K α Comparison with Chandra and XMM-Newton

Historical variability of the Fe-K α line intensity is useful to diagnose the location of the fluorescing matter. We begin with a comparison with the archival XMM-Newton data taken in 2001 and 2006. The procedures of the data reduction as described below are based on the XMM-Newton ABC guide.³ The raw PN and MOS data are reprocessed using the pipelines `epchain` and `emchain`, respectively.

We filter the duration where the background activity is high, judged from the background light curve in the 10–12 keV band. We also impose the event pattern selection $\text{PATTERN} \leq 4$ (single and double events) for PN and $\text{PATTERN} \leq 12$ (single, double, triple, and quadruple events) for MOS. To determine the source region, pile-up is checked with the SAS tool `epatplot`, and we find it is significant in the vicinity of the AGN. Hence, depending on its strength, on-core 7''–14'' and 8''–14'' annular regions are adopted for the 2001 and 2006 data, respectively, to exclude the pixels suffering from pile-up. Note that the PN data in 2006 is not used because the pile-up affects the entire extraction region for NGC 1275. The background spectra including the ICM emission is estimated from a 60''–63'' annular region following Yamazaki et al. (2013). We combine the spectra from the two individual MOS detectors.

Our main focus is accurate measurement of the Fe-K α flux, and thus we have to determine the continuum

² `sxt-s-PSFimage_150120.fits` packed in the `simx` v2.4.1 package.

³ (<https://heasarc.gsfc.nasa.gov/docs/xmm/abc/>).

Table 3. Results of the spectral fits to the XMM-Newton, Chandra/HEG, and Chandra/ACIS spectra in the 4–8 keV band.

Component	Parameter	XMM-Newton/PN and MOS in 2001	XMM-Newton/MOS in 2006	Chandra/HEG in 1999 (simultaneous fitting)	Chandra/HEG in 2000 (simultaneous fitting)
constant	C_{inst}	0.85 ± 0.07
powerlaw	Γ	1.24 ± 0.19	1.50 ± 0.14	0.76 ± 0.58	$2.01^{+0.48}_{-0.47}$
	N_{PL}^*	$1.35^{+0.50}_{-0.36}$	$2.79^{+0.73}_{-0.58}$	$0.56^{+0.90}_{-0.35}$	$9.81^{+11.23}_{-5.20}$
zgauss	E (keV)		6.40 (fix)		
	σ (eV)		10 (fix)		
	z		0.017284 (fix)		
	$N_{\text{zgauss}}^\dagger$	$12.59^{+6.22}_{-5.90}$	$13.26^{+6.01}_{-5.79}$	$2.35^{+6.74}_{-2.35}$	
C-statistics/d.o.f.		1418.03/1445	820.86/788	615.14/789	
Component	Parameter	Chandra/ACIS in 2004 (simultaneous fitting)			
apec	T_e (keV)	4.22 ± 0.09			
	A (solar)	0.47 ± 0.01			
	z_{apec}	0.017284 (fix)			
	N_{apec}^\ddagger	3.70 ± 0.08			
zgauss	E (keV)	6.40 (fix)			
	σ (eV)	10 (fix)			
	z_{zgauss}	$=z_{\text{apec}}$			
	$N_{\text{zgauss}}^\ddagger$	$1.90^{+1.50}_{-1.49}$			
C-statistics/d.o.f.		3232.51/2999			

*The powerlaw normalization at 1 keV, in units of 10^{-3} photons keV $^{-1}$ cm $^{-2}$ s $^{-1}$.

† The zgauss normalization, in units of 10^{-6} photons cm $^{-2}$ s $^{-1}$.

‡ The apec normalization, in units of $\{10^{-16}/4\pi[D_A(1+z)]^2\} \int n_e n_H dV$, where D_A is the angular size distance to the source (cm), and n_e and n_H are the electron and H densities (cm $^{-3}$).

level with the least bias. For that purpose, we analyze the 4–8 keV spectra to reduce the systematic uncertainty caused by the ICM emission subtraction. The spatial variation of the ICM emission also makes suitable background subtraction difficult. The RMFs and ARFs are generated in a standard manner appropriate to a point source. We fit these data with a model consisting of a power-law continuum and a Gaussian Fe-K α emission line (powerlaw + zgauss). When fitting the PN and MOS spectra in 2001, the systematic uncertainty between the two is taken into consideration by applying the constant model to the total (C_{inst} in table 3). The photon index and normalization of the powerlaw, and the normalization of the zgauss, are left free, while the line energy, its width, and the redshift of zgauss are fixed at 6.4 keV, 10 eV, and 0.017284, respectively. Table 3 and figure 4 summarize the fitting results. The Fe-K α fluxes are measured to be $(12.59^{+6.22}_{-5.90}) \times 10^{-6}$ photons cm $^{-2}$ s $^{-1}$ in 2001, and $(13.26^{+6.01}_{-5.79}) \times 10^{-6}$ photons cm $^{-2}$ s $^{-1}$ in 2006 (errors are 90% confidence). The line fluxes are in good agreement with that in 2016 obtained from the Hitomi data despite the significant brightening of the AGN continuum (powerlaw) emission indicating a lack of immediate response of the line to continuum changes.

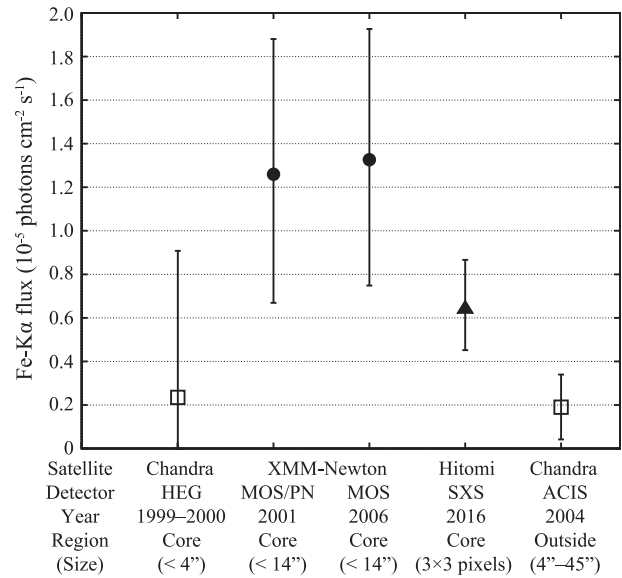


Fig. 4. Comparison of the Fe-K α fluxes among different satellites, instruments, years, and regions. Open squares, filled circles, and filled triangle show the Fe-K α fluxes obtained by Chandra, XMM-Newton, and Hitomi, respectively. Error bars show 90% confidence ranges.

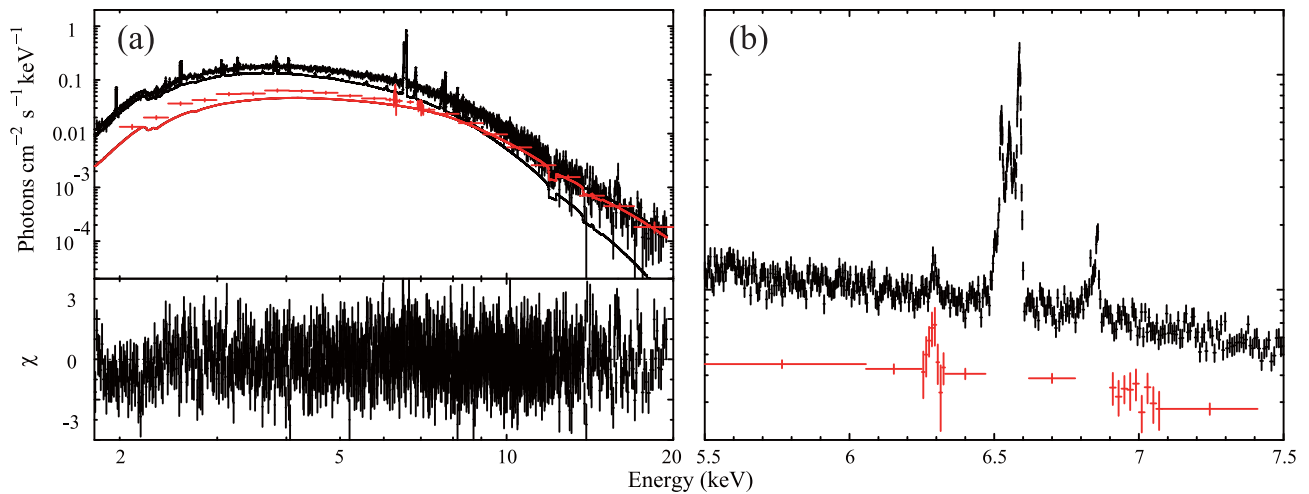


Fig. 5. (a) Broad-band spectrum obtained by the nine SXS on-core pixels, fitted with the model of the ICM plus AGN emission. Black is the on-core nine-pixel SXS spectrum, while red is the spectrum of NGC 1275 derived by the PSF photometry method. The black and red solid lines are the best-fit *bbvapec* and *pegwrlw* components, respectively, derived by the fit to only the SXS on-core nine-pixel spectrum. (b) Enlargement of panel (a) around the Fe-K α line region without the models. (Color online)

To extract the AGN spectra from the HEG data, we run `chandra_repro` with the default parameter set. There is no evidence for pile-up using the CIAO tool `pileup_map`. The source region is a rectangle surrounding dispersed X-rays with a width of $\sim 4''.8$, whereas that for the background including the ICM emission is two rectangles with a width of $\sim 22''$ located on either side along the source region. The RMFs and ARFs are produced by assuming a point source. To get a stronger constraint on the Fe-K α flux, we simultaneously fit the 4–8 keV spectra in 1999 and 2000 using the model of `powerlaw` + `zgauss`. We determine the continuum component (`powerlaw`) independently in the two spectra but tie the Fe-K α line intensity. The resultant intensity is $(2.35^{+6.74}_{-2.35}) \times 10^{-6}$ photons $\text{cm}^{-2} \text{s}^{-1}$, consistent with those in the XMM-Newton (2001 and 2006) and Hitomi (2016) observations.

In the same manner as for the Chandra/HEG data, we reprocess the Chandra/ACIS data, and find that while the nuclear region ($<4''$) is badly affected by pile-up, the outer regions are not affected. Hence, the Chandra/ACIS allows us to investigate if there is an Fe-K α source other than the AGN. The SXS pixel distribution of the Fe-K α flux has already limited the extent of the Fe-K α emitter to be $\lesssim 42''$, so we use the Chandra/ACIS data to constrain the flux in the $4''$ – $45''$ annular region around the AGN. The background region is a $50''$ circle, where no other source is present. The 4–8 keV spectra are extracted from all the Chandra/ACIS archival data listed in table 1. With RMFs and ARFs optimized for the extended source, we perform a simultaneous fitting to the 11 spectra with a model consisting of thermal plasma emission from the ICM and a neutral Fe-K α line (`apec` + `zgauss`). All parameters in the ICM

model except for the redshift of 0.017284 (i.e., the electron temperature, elemental abundance, and normalization) are left free, while `zgauss` is treated in the same manner in the HEG analysis. The neutral Fe-K α line flux is constrained to be $(1.90^{+1.50}_{-1.49}) \times 10^{-6}$ photons $\text{cm}^{-2} \text{s}^{-1}$. Although the detection is significant at $\sim 97\%$ confidence level, the resultant flux is significantly smaller than those measured with XMM-Newton/MOS and PN and Hitomi/SXS. We conclude that the Fe-K α emission in the region in the $4''$ – $42''$ annulus from the core does not significantly contribute to the Hitomi detection and thus the Fe-K α flux observed with the SXS comes mainly from the nucleus region within a $4''$ radius, or ~ 1.6 kpc from NGC 1275. Hence, the Fe-K α emitter is likely located within the circumnuclear material.

3.2 Broad-band spectral analysis

3.2.1 Direct fit to the SXS on-core nine-pixel spectrum

We now turn to a broad-band spectral analysis of the SXS data in order to constrain the AGN continuum. This requires a careful decomposition of the spectrum into ICM and AGN components; indeed, the spectrum of the AGN is important for any detailed studies of ICM emission. Because the spectral continuum of the AGN is different from that of the ICM, it is effective to study the broadest band possible. In spite of its being, nominally, a soft X-ray instrument, the combination of the SXT + SXS possesses sufficient sensitivity to detect NGC 1275 at ~ 20 keV. At such high energies the AGN dominates the SXS signal (see figure 5). The fact that the SXS gate valve was still closed during this observation limits the analysis to energies above 1.8 keV. We use the same RMF as in sub-subsection 3.1.1 (see subsection 2.1).

Table 4. Results of the fits to the SXS on-core nine-pixel spectrum and the PSF photometry spectrum in the baseline case, and in the cases utilizing the ARFs corresponding to the ground and orbital calibration.

Component	Parameter	Baseline	Ground calibration	Orbital calibration
Direct fit to the SXS on-core nine-pixel spectrum				
pegpwr1w	Γ	$1.60^{+0.13}_{-0.15}$	$1.99^{+0.07}_{-0.10}$	$1.71^{+0.10}_{-0.11}$
	$F_{2-10\text{ keV}}^*$	$2.31^{+0.40}_{-0.35}$	$3.93^{+0.42}_{-0.49}$	$3.05^{+0.41}_{-0.39}$
zgauss $\times 2$	EW (eV)	$26.5^{+3.7}_{-3.1}$	$16.4^{+1.6}_{-1.1}$	$20.7^{+2.3}_{-1.9}$
C-statistics/d.o.f.		10562.2/11120	10559.6/11120	10560.9/11120
Fit to the PSF-photometry spectrum				
pegpwr1w	Γ	1.83 ± 0.04	1.79 ± 0.04	1.76 ± 0.04
	$F_{2-10\text{ keV}}^*$	2.97 ± 0.06	2.85 ± 0.06	2.98 ± 0.06
zgauss $\times 2$	EW (eV)	20.3 ± 0.3	20.9 ± 0.3	19.8 ± 0.3
$\chi^2/\text{d.o.f.}$		21.0/39	25.2/39	20.1/39

*The 2–10 keV flux of the `pegpwr1w` in units of $10^{-11} \text{ erg cm}^{-2} \text{ s}^{-1}$.

We use the diffuse and point-like source ARFs for the ICM and AGN model component, respectively. The ARF for the AGN model is same as that used in sub-subsection 3.1.1 (see subsection 2.1).

We perform the direct fit to the 1.8–20 keV spectrum from the 3×3 pixel (#0–#8) region of the SXS centered on the AGN, which is the same as that in sub-subsection 3.1.1, with a model consisting of ICM and AGN components. Both the ICM and AGN components are modified by the effects of Galactic absorption (described using the XSPEC model `TBabs`) with a column density of $1.38 \times 10^{21} \text{ cm}^{-2}$ derived from the Leiden/Argentine/Bonn (LAB) Survey of Galactic H I (Kalberla et al. 2005). The ICM emission is modeled with `zshift*bvvapec`, which is the redshifted thermal plasma model including thermal and turbulent line broadening, together with `AtomDB` version 3.0.9.⁴ Avoiding the mismatch of line ratio due to resonance scatterings (Hitomi Collaboration 2018b), we exclude the `FeXXV He α` resonance line from the model, and instead we introduce one Gaussian model to represent this resonance line. Hence, the model fitted to the ICM is `TBabs*zshift*bvvapec + gauss`. Light elements, He through to Al, are assumed to have solar abundances (as defined by Lodders & Palme 2009) because the relevant lines of these elements are out of the SXS energy range. The abundance of other elements are allowed to be non-solar, but those of P, Cl, K, Sc, Ti, V, Co, Cu, and Zn are all tied to that of Fe, following Hitomi Collaboration (2018c). The AGN component is modeled by a power law plus the iron fluorescence lines (`Fe-K α_1 +Fe-K α_2`), `pegpwr1w + zgauss`

+ `zgauss`, where the normalization ratio of two Gaussians is fixed to 1 : 2 as described in sub-subsection 3.1.1. We perform the spectral fit in the energy range of 1.8–20 keV with C-statistics. The spectrum is grouped so as to have at least one photon in each channel.

As a result, the SXS spectrum is well fitted by this model with C-statistics/d.o.f. = 10562.2/11120, as shown in figure 5a. The direct fit results of the AGN parameters are summarized in the Baseline column of table 4. The ICM parameters become $z_{\text{ICM}} = 0.01729^{+0.00002}_{-0.00004}$, $T_e = 3.82 \pm 0.07 \text{ keV}$, and $V_{\text{turb}} = 158.6^{+11.7}_{-11.9} \text{ km s}^{-1}$, which are almost consistent with those reported by Hitomi Collaboration (2018a, 2018c). The ICM abundance values of the various elements are summarized in table 5, and their ratios are confirmed to be consistent with those reported in Hitomi Collaboration (2017). Hence, we do not discuss the ICM parameters any further in the present paper.

3.2.2 Analyses of the PSF photometry spectrum

Although the statistical errors on the AGN spectral slope and flux are rather small, as shown in table 4, they are correlated with the ICM parameters, and potentially susceptible to systematics resulting from uncertainties in the calibration and modeling. In fact, the power-law photon index is distributed widely from 1.4 to 2.2 when we use the different gain calibration, RMF size, and ARF effective area.⁵ This is because the AGN component is buried in the

⁴ Because treatments of some Fe-K lines are updated from `AtomDB` version 3.0.8, we use version 3.0.9 in the present paper. APEC versions 3.0.8 and 3.0.9 produce just a small difference in the photon index of ~ 0.05 in the AGN spectral fitting.

⁵ Note that, as described in subsection 2.1, we use the additional gain calibration in addition to that used in the default pipeline processing of the SXS data. Furthermore, there are four options on the RMF size in the SXS RMF generator `sxsmkrmf`. These RMFs are different not only in size but also some response issues considered in the calculation. See sub-subsection 3.2.2 for the systematic errors due to the ARF effective area.

Table 5. Abundance values of the ICM modeled by *bvvapec* in the direct fit to the SXS on-core nine-pixel spectrum.*

Element	Abundance (solar)
Si	$0.67^{+0.13}_{-0.12}$
P	$=A_{\text{Fe}}$
S	$0.75^{+0.09}_{-0.07}$
Cl	$=A_{\text{Fe}}$
Ar	$0.64^{+0.08}_{-0.09}$
K	$=A_{\text{Fe}}$
Ca	$0.71^{+0.10}_{-0.08}$
Sc	$=A_{\text{Fe}}$
Ti	$=A_{\text{Fe}}$
V	$=A_{\text{Fe}}$
Cr	$0.35^{+0.23}_{-0.22}$
Mn	$0.54^{+0.35}_{-0.33}$
Fe	$0.65^{+0.06}_{-0.05}$
Ni	$0.71^{+0.14}_{-0.13}$
Cu	$=A_{\text{Fe}}$
Zn	$=A_{\text{Fe}}$

* A_{Fe} is the Fe abundance in units of solar abundance.

ICM emission, especially below 6 keV, and hence the spectral slope can be significantly affected by a small change of the calibration and modeling. Therefore, we perform a model-independent evaluation of the AGN spectrum via the image analysis, employing the PSF photometry on the SXS pixel maps derived in multiple narrow energy bands (see appendix 1 for further details of the creation of the PSF photometry spectrum). The derived PSF photometry spectrum is shown in figure 5a. It is successfully determined up to 20 keV, and the Fe-K α line also clearly appears as shown in figure 5b.

We fit the PSF photometry spectrum with an absorbed power-law model with two Gaussians modeled as $\text{TBabs}*(\text{pegpwr1w} + \text{zgauss} + \text{zgauss})$.⁶ We fix the Galactic absorption column density to that used in the direct fit in sub-subsection 3.2.1. Because the bin size of the PSF photometry spectrum is much larger than that of the SXS on-core nine-pixel spectrum, we fix the parameters of two Gaussians at the best-fit values with the gain corrections in table 3. Because the errors given by the PSF photometry method (see appendix 1) do not follow a Poisson distribution, we use χ^2 statistics in place of C -statistics. As shown by the Baseline column in table 4,

the fit is successful with $\chi^2/\text{d.o.f.} = 21.0/39$, and the *pegpwr1w* photon index and flux in 2–10 keV become 1.83 ± 0.04 and $(2.97 \pm 0.06) \times 10^{-11} \text{ erg cm}^{-2} \text{ s}^{-1}$, respectively. The EW of the Fe-K α line against the AGN continuum becomes $20.3 \pm 0.3 \text{ eV}$. Incorporating the PSF photometry method, we thus obtain an AGN spectrum which is slightly steeper than that derived by the direct fit in sub-subsection 3.2.1. Note that these AGN parameters based on the PSF photometry manner are employed in the other Hitomi papers of the Perseus cluster of galaxies (Hitomi Collaboration 2017, 2018a, 2018b, 2018c, 2018d).

3.2.3 Broad-band comparison with Chandra and XMM-Newton including systematic errors

Finally, in order to compare the AGN parameters in 2016 with those from the previous occasions by the different satellites, we check parameter changes due to the effective area uncertainties, which mainly produce large systematic errors. The effective area calculated by *aharfgen* is different from that measured in the ground calibration by up to $\sim 7\%$ (Hitomi Collaboration 2018a, 2018d), and that investigated in the orbital calibration by utilizing the Crab ratio by up to $\sim 10\%$ (Tsujiimoto et al. 2018; Hitomi Collaboration 2018a, 2018d). Then, we modify the ARF according to the differences from the ground and orbital calibration individually, and again perform the fits to the SXS on-core nine-pixel spectrum and the PSF photometry spectrum. The results are summarized in table 4. Consequently, considering the systematic uncertainties of the direct fits, which are wider than those in the fits to the PSF photometry spectrum, the parameter range of the power-law photon index is determined to be 1.45–2.06. The 2–10 keV flux range is $(1.96\text{--}4.35) \times 10^{-11} \text{ erg cm}^{-2} \text{ s}^{-1}$, which is comparable to the AGN brightness around the 1980s–1990s (Fabian et al. 2015). The range of the Fe-K α EW against the AGN continuum becomes 15.3–30.2 eV.

How different are the AGN spectral shape and flux obtained by the SXS in 2016 from those in the past X-ray observations? First, we check the Chandra/HEG 0.5–7 keV spectra obtained in 1999 and 2000 (see table 1). The Chandra/HEG source and background spectra, the RMFs, and ARFs are all the same as those in sub-subsection 3.1.3, but the energy band is changed to 0.5–7 keV. We fit the HEG spectra with the model of $\text{TBabs}*(\text{pegpwr1w} + \text{zgauss})$, where the parameter settings of *TBabs* and *pegpwr1w* are the same as in sub-subsection 3.2.2, while those of *zgauss* are fixed at the values with the gain corrections in table 3 except for its normalization, which is left free. As shown in table 6, the fits are successful, and the 2–10 keV flux in 1999 is significantly lower than 2016, while that in 2000 is compatible with 2016.

⁶ Because we do not use *AtomDB* in the fit to the PSF photometry spectrum, the results in this subsection are not related to the *AtomDB* version update.

Table 6. Results of the fits to the 0.5–7 keV Chandra/HEG and 0.7–8 keV XMM-Newton spectra.

Component	Parameter	Chandra/HEG in 1999	Chandra/HEG in 2000	XMM-Newton/PN and MOS in 2001	XMM-Newton/MOS in 2006
pegpwr1w	Γ	1.66 ± 0.07	2.12 ± 0.05	1.74 ± 0.02	$1.75^{+0.02}_{-0.01}$
	$F_{2-10 \text{ keV}}^*$	1.05 ± 0.07	2.44 ± 0.11	1.17 ± 0.03	1.56 ± 0.03
C-statistics/d.o.f.		2857.4/3537	2937.1/3655	2707.7/2768	1591.5/1447

*The 2–10 keV flux of *pegpwr1w* in units of $10^{-11} \text{ erg cm}^{-2} \text{ s}^{-1}$.

The XMM-Newton broad-band spectra in 2001 and 2006 were already reported by Churazov et al. (2003) and Yamazaki et al. (2013), respectively. However, as shown in sub-subsection 3.1.3, we utilize different source- and background-extraction regions to avoid pile-up effects, and hence we reanalyze the 0.7–8 keV spectra in both 2001 and 2006. The source and background spectral files, the RMS and ARFs, are identical to those in sub-subsection 3.1.3, and the energy band is broadened to 0.7–8 keV. We fit the MOS and PN spectra simultaneously in 2001, while only the MOS spectrum in 2006, using the model of *TBabs*(pegpwr1w + zgauss)* with the same parameter settings as those in the Chandra/HEG 0.5–7 keV analyses. The fits are both successful, as shown in table 6, and their 2–10 keV fluxes become between those by Chandra/HEG in 1999 and 2000, and significantly lower than that by SXS in 2016. Comparing the results by the Chandra/HEG, XMM-Newton, and the SXS with the systematic errors, the relation between the photon index and the flux of the AGN continuum is confirmed to be consistent with the trend of “steeper when brighter,” which is often seen in the AGN slope variability.

4 Discussion

4.1 The origin of the Fe-K α line from NGC 1275

The Fe-K α velocity width of $\sim 500\text{--}1600 \text{ km s}^{-1}$ (sub-subsection 3.1.1) is significantly below that of the broad H α emission line ($\sim 2750 \text{ km s}^{-1}$) reported by Ho et al. (1997). Applying simple Keplerian arguments (assuming that the black hole mass of $8 \times 10^8 M_{\odot}$ dominates the potential and that the distribution is an edge-on disk) suggests that the fluorescing matter is $\sim 1.4\text{--}14 \text{ pc}$ from the black hole—the inclusion of the stellar mass and finite inclination effects would further increase this distance estimate. We conclude that the matter responsible for the Fe-K α emission line in NGC 1275 is exterior to the BLR, possibly being associated with the dusty torus of unification schemes, or the circumnuclear molecular disk (Scharwächter et al. 2013). Furthermore, the inner parts of the cluster-scale CO clouds illuminated by the ICM X-ray emission should also be considered as a possible site, because they were reported to have

a velocity field which matches that derived in the present study (Salomé et al. 2006). The cluster-scale origin of Fe-K α line emission was originally predicted by Churazov et al. (1998), and also discussed by Fabian et al. (2015).

The constraint imposed by the SXS pixel map (sub-subsection 3.1.2) and the Chandra imaging (sub-subsection 3.1.3), namely that the line emission is within 1.6 kpc of NGC 1275, firmly places the fluorescing material in the region where the AGN continuum (as opposed to the ICM emission) is the dominant source of irradiation that drives the fluorescence. Thus, we can essentially rule out dominant contributions from the extended CO clouds illuminated by the ICM X-ray emission. Although the CO molecular clouds in the centrally concentrated region within 1.6 kpc (Salomé et al. 2006) could be illuminated by the AGN emission, we confirm that the Fe-K α flux from them is too small (the EW is just less than 0.15 eV) to explain the Hitomi observed Fe-K α flux, by incorporating Monte Carlo simulation (see appendix 2 for details). As Chandra might have detected the Fe-K α line from the $4''\text{--}45''$ region with a $\sim 97\%$ confidence level, a relatively small fraction of the line flux detected by Hitomi could be produced by the CO gas irradiated by collimated and beamed X-rays from a relativistic jet observed in NGC 1275 (Abdo et al. 2009). This possibility is discussed in subsection 4.2.

The Fe-K α line flux is found to be almost constant over a 16 yr duration from the 1999–2000 Chandra to the 2016 Hitomi datapoints (sub-subsection 3.1.3), despite the flux change of the power-law continuum by an order of magnitude shown in Fabian et al. (2015). The most obvious interpretation for the lack of line variability is to invoke light travel time effects in an extended source. Depending upon the precise geometry, the lack of time variability and the width of the Fe-K α lines are consistent with a source of at least $\sim 5 \text{ pc}$. Of the known structures within the NGC 1275 system, we conclude that the most likely origin of the fluorescent Fe-K α line is the putative dusty torus, or the observed circumnuclear molecular disk which extends to distances of 50–100 pc from the black hole (Scharwächter et al. 2013). However, the dusty torus, if it is present, would have a relatively low column density and/or low covering fraction, and be rather different from that assumed in other works on the Fe-K α line in Seyfert galaxies, because the EW

of the Fe-K α line in NGC 1275 is $\gtrsim 5$ times less than what typical Seyferts have. This is consistent with the picture that AGNs with low Eddington ratios (which may include NGC 1275 with $L_B/L_{\text{Edd}} \sim 3 \times 10^{-4}$; Sikora et al. 2007) have low covering fractions of the dusty torus (e.g., Kawamuro et al. 2016; Ramos Almeida & Ricci 2017; Ricci et al. 2017). This point is also discussed in subsection 4.3.

If we assume that the structure is Compton thin, we can “count” fluorescing atoms to obtain an estimate of the mass of cold gas in this structure. Following the simple analytic arguments of Reynolds, Nowak, and Maloney (2000) to relate the (average) EW of the fluorescent line W_{Fe} to the column density N_{H} , iron abundance Z_{Fe} , and covering fraction f_{cov} of the fluorescing material as seen from the AGN, we obtain

$$W_{\text{Fe}} \approx 65 f_{\text{cov}} \left(\frac{Z_{\text{Fe}}}{Z_{\odot}} \right) \left(\frac{N_{\text{H}}}{10^{23} \text{ cm}^{-2}} \right) \text{ eV}. \quad (1)$$

Taking the Hitomi value of $W_{\text{Fe}} \approx 20 \text{ eV}$, which is derived against only the AGN continuum (table 4), and assuming solar abundances for the circumnuclear matter, we conclude that $N_{\text{H}} f_{\text{cov}} \approx 3.0 \times 10^{22} \text{ cm}^{-2}$. Placing this matter at a distance of $r = 100 \text{ pc}$ from the AGN, the resulting total mass of gas is $M = 4\pi r^2 f_{\text{cov}} N_{\text{H}} \mu m_p$, which evaluates to $M \sim 4 \times 10^7 M_{\odot}$. To put this number into perspective, if this material were to undergo efficient accretion into the central SMBH, it could power the observed AGN for about a Hubble time. If the accretion were highly inefficient (say 0.1%), this quantity of gas could power the observed AGN for approximately an ICM core cooling time. We note that Scharwächter et al. (2013) estimated the electron density of the [Fe II] emitters to be $\sim 4000 \text{ cm}^{-3}$. For this to be consistent with our conclusions requires either a small covering fraction ($f_{\text{cov}} \approx 0.02$), a clumpy or shell-like medium, or both.

4.2 Consideration of multi-wavelength results

NGC 1275 has a relatively high $12 \mu\text{m}$ luminosity from the central $\sim 100 \text{ pc}$ region (Asmus et al. 2016), and the ratio between the X-ray and mid-infrared (MIR) is consistent with that expected from the X-ray and MIR luminosity relation in AGN with normal dusty tori (Ichikawa et al. 2017). Hence, the MIR luminosity apparently supports the presence of a normal dusty torus, and that picture looks inconsistent with the picture obtained in subsection 4.1. However, because NGC 1275 is a well-known GeV/TeV gamma-ray emitter (Abdo et al. 2009; Aleksić et al. 2012), the jet emission could strongly contribute to the MIR band, and a large fraction of the MIR luminosity could be explained by the jet emission. If so, the normal dusty torus is not required, and the picture is thus consistent with that in

subsection 4.1. To examine whether or not the jet emission significantly contributes to the MIR band, we need further studies of the spectral energy distribution (SED) of the jet emission.

If strongly beamed jet X-ray emission, which is out of our line of sight, could illuminate a part of the CO molecular clouds extended outside the AGN (Salomé et al. 2006), high Fe-K α line flux might be generated, even though the solid angle of the clouds from the central engine is small. From the gamma-ray observations, the jet power of NGC 1275 has been estimated to be $\sim 10^{44} \text{ erg s}^{-1}$ (Abdo et al. 2009) or higher (Tavecchio & Ghisellini 2014), and hence the X-ray luminosity of the beamed jet reaches $\gtrsim 10^{43-44} \text{ erg s}^{-1}$. This could produce the Fe-K α line flux enough to explain EW $\sim 20 \text{ eV}$ against the jet X-ray continuum with a luminosity of $\sim 10^{43} \text{ erg s}^{-1}$. Thus, this picture may explain all or some fraction of the observed Fe-K α line flux with neither a dusty torus nor a circumnuclear molecular disk in NGC 1275. In order to test this, understanding of the SED of the jet component are important as well as detailed studies of the velocity field of the extended molecular clouds.

Furthermore, we consider the possible contribution of the proton-induced Fe-K α line. Such an origin has been suggested to explain the diffuse 6.4 keV line at the Galactic center (Nobukawa et al. 2015). At the central region of NGC 1275, cosmic-ray protons could be enhanced by jet-induced shock acceleration (Kino et al. 2016). By assuming a proton energy spectrum with an index of -2.5 and an energy density of 20 eV cm^{-3} in 0.1–1000 MeV, Nobukawa et al. (2015) estimated the intensity of the proton-induced Fe-K α line to be $I_{6.4 \text{ keV}} = 6.6 \times 10^{35} (N_{\text{H}}/10^{24} \text{ cm}^{-2}) (U_p/20 \text{ eV cm}^{-3}) \times (S/1 \text{ pc}^2) \text{ erg s}^{-1}$. Because the Fe-K α flux derived by the SXS corresponds to the much higher luminosity of $\sim 7 \times 10^{40} \text{ erg s}^{-1}$, we find that the nominal proton energy density of several eV cm^{-3} cannot explain the Hitomi result, and a much broader region needs to be illuminated by MeV protons with much higher energy density. However, we need further limitations of the geometry of proton injection and molecular clouds to more accurately estimate the proton-induced Fe-K α flux.

4.3 Comparison with other types of AGN

The origin of the Fe-K α line of NGC 1275 in 2016, possibly identified to be the low covering fraction and/or low column density torus, or the circumnuclear molecular disk, is clearly distinct from those in normal Seyfert galaxies claimed to be located at a region inside the dusty torus (e.g., Shu et al. 2010, 2011). This may reflect some distinction of BLR and dusty torus structures between NGC 1275 and Seyfert galaxies. A BLR should be present in 2016, because

NGC 1275 was at comparable flux in the Hitomi observations to that of the early 1980s when the broad H α line was detected (Ho et al. 1997), and contemporaneous HST optical data derived on 2016 January 7 show a composite H α line whose profile is similar to that reported by Ho et al. (1997). Thus, we expect a BLR FWHM of $\sim 2750 \text{ km s}^{-1}$ in 2016, which rules out a large contribution of the BLR to the much narrower Hitomi Fe-K α line.

Although we do not have other information relevant to whether a torus was present during the Hitomi observations, the Eddington ratio might drive the structure of the dusty torus as inferred by Kawamuro et al. (2016). When an AGN is less luminous than the critical luminosity, its dusty torus might not be able to sufficiently inflate and cover a large enough solid angle to produce a high EW Fe-K α line. Presumably related to this, Ramos Almeida and Ricci (2017) and Ricci et al. (2017) showed that the fraction of the obscured AGN decreases with $L_B \lesssim 10^{42} \text{ erg s}^{-1}$ and $L_B/L_{\text{Edd}} \lesssim 10^{-4}$, respectively. Our results show that NGC 1275 follows this pattern like other low-luminosity AGN, and thus its Fe-K α line profile might be different from those from normal Seyfert galaxies.

Another possibility is that AGN emission line structures are different in radio-loud and radio-quiet AGN even when their luminosities are similar. This picture is consistent with the fact that the amounts of reflection, strength, and width of the Fe-K α lines are different in radio-loud AGN (e.g., Tazaki et al. 2011, 2013). Because of the lower EW of Fe-K α lines and lower X-ray fluxes, the study of Fe-K α line emission in radio-loud AGN at high energy resolution with the Chandra gratings has been difficult except for a few of the brightest sources (e.g., Tombesi et al. 2016). Thus, X-ray microcalorimeters on board future satellites, such as the X-ray Astronomical Recovery Mission (XARM) and the Athena X-ray observatory, are essential for further work in this field, as shown by the ability of the SXS on board Hitomi to detect the weak emission line with EW $\sim 9 \text{ eV}$ in NGC 1275, the fiftieth brightest AGN.

5 Conclusion

The SXS on board the Hitomi satellite detected and resolved the fluorescence Fe-K α line emission from the radio galaxy NGC 1275 at the center of the Perseus cluster of galaxies. This is the first observation of the Fe-K α line from an AGN with the unprecedentedly high energy resolution of $\sim 6.4 \text{ keV}$ provided by an X-ray microcalorimeter. The well-constrained line velocity width of $500\text{--}1600 \text{ km s}^{-1}$ allows us to rule out the possibility that the Fe-K α line originates from an accretion disk and a BLR. Moreover, analyzing the Chandra archival data, we can limit the outer boundary of the Fe-K α source region to be within $\sim 1.6 \text{ kpc}$ of the central engine. Taking into account the

small EW of the Fe-K α line $\sim 20 \text{ eV}$ against the AGN continuum, the lack of time variability of the line, and its low physical width, the origin of the Fe-K α line is likely to be a low covering fraction and/or low column density molecular torus or a circumnuclear molecular disk associated with infrared [Fe II] lines, unlike normal Seyfert galaxies. The present result demonstrates the power of X-ray microcalorimeter spectroscopy of AGN Fe-K α lines, even if the lines are very weak with EW $\sim 9 \text{ eV}$. Future XARM and Athena observations are expected to bring us many discoveries and important results in AGN science.

Author contributions

H. Noda led this study, analyzed the SXS data, and wrote the manuscript, along with Y. Fukazawa, R. F. Mushotzky, and C. S. Reynolds. H. Noda and F. S. Porter contributed to the SXS hardware development, including designs, integrations, performance tests, launch campaign, and in-orbit operation. F. S. Porter and S. Nakashima contributed to the in-orbit calibration of the SXS. Y. Fukazawa performed the SXS pixel map analyses and the PSF photometry method. K. Hagino worked on the Monte Carlo simulation and its interpretation. T. Kawamuro performed the analyses of the Chandra and XMM-Newton archival data. H. Noda, Y. Fukazawa, R. F. Mushotzky, C. S. Reynolds, T. Tanaka, T. Kawamuro, L. W. Brenneman, F. Tombesi, H. Seta, A. C. Fabian, M. Ohno, and C. Done contributed to the discussion and interpretation parts. L. C. Gallo, C. Pinto, M. Loewenstein, P. Gandhi, T. Yaqoob, M. Guainazzi, M. Tsujimoto, and N. Yamasaki helped to improve the manuscript.

Acknowledgments

We acknowledge the support from the JSPS Core-to-Core Program, and all the JAXA members who have contributed to the ASTRO-H (Hitomi) project. All US members gratefully acknowledge support through the NASA Science Mission Directorate. Stanford and SLAC members acknowledge support via DoE contract to SLAC National Accelerator Laboratory DE-AC3-76SF00515. Part of this work was performed under the auspices of the US DoE by LLNL under Contract DE-AC52-07NA27344. Support from the European Space Agency is gratefully acknowledged. The French members acknowledge support from CNES, the Centre National d'Études Spatiales. SRON is supported by NWO, the Netherlands Organization for Scientific Research. The Swiss team acknowledges the support of the Swiss Secretariat for Education, Research and Innovation (SERI). The Canadian Space Agency is acknowledged for the support of Canadian members. We acknowledge support from JSPS/MEXT KAKENHI grant numbers 15J02737, 15H00773, 15H00785, 15H02090, 15H03639, 15H05438, 15K05107, 15K17610, 15K17657, 16J00548, 16J02333, 16H00949, 16H06342, 16K05295, 16K05296, 16K05300, 16K13787, 16K17672, 16K17673, 21659292, 23340055, 23340071, 23540280, 24105007, 24244014,

24540232, 25105516, 25109004, 25247028, 25287042, 25400236, 25800119, 26109506, 26220703, 26400228, 26610047, 26800102, JP15H02070, JP15H03641, JP15H03642, JP15H06896, JP16H03983, JP16K05296, JP16K05309, JP16K17667, and JP16K05296. The following NASA grants are acknowledged: NNX15AC76G, NNX15AE16G, NNX15AK71G, NNX15AU54G, NNX15AW94G, and NNG15PP48P to Eureka Scientific. H. Akamatsu acknowledges the support of NWO via a Veni grant. C. Done acknowledges STFC funding under grant ST/L00075X/1. A. Fabian and C. Pinto acknowledge ERC Advanced Grant 340442. P. Gandhi acknowledges JAXA International Top Young Fellowship and UK Science and Technology Funding Council (STFC) grant ST/J003697/2. Y. Ichinohe, K. Nobukawa, and H. Seta are supported by the Research Fellow of JSPS for Young Scientists. N. Kawai is supported by the Grant-in-Aid for Scientific Research on Innovative Areas “New Developments in Astrophysics Through Multi-Messenger Observations of Gravitational Wave Sources.” S. Kitamoto is partially supported by the MEXT Supported Program for the Strategic Research Foundation at Private Universities, 2014–2018. B. McNamara and S. Safi-Harb acknowledge support from NSERC. T. Dotani, T. Takahashi, T. Tamagawa, M. Tsujimoto, and Y. Uchiyama acknowledge support from the Grant-in-Aid for Scientific Research on Innovative Areas “Nuclear Matter in Neutron Stars Investigated by Experiments and Astronomical Observations.” N. Werner is supported by the Lendület LP2016-11 grant from the Hungarian Academy of Sciences. D. Wilkins is supported by NASA through Einstein Fellowship grant number PF6-170160, awarded by the Chandra X-ray Center, operated by the Smithsonian Astrophysical Observatory for NASA under contract NAS8-03060.

We acknowledge the contributions by many companies, including, in particular, NEC, Mitsubishi Heavy Industries, Sumitomo Heavy Industries, and Japan Aviation Electronics Industry. Finally, we acknowledge strong support from the following engineers. JAXA/ISAS: Chris Baluta, Nobutaka Bando, Atsushi Harayama, Kazuyuki Hirose, Kosei Ishimura, Naoko Iwata, Taro Kawano, Shigeo Kawasaki, Kenji Minesugi, Chikara Natsukari, Hiroyuki Ogawa, Mina Ogawa, Masayuki Ohta, Tsuyoshi Okazaki, Shin-ichiro Sakai, Yasuko Shibano, Maki Shida, Takanobu Shimada, Atsushi Wada, Takahiro Yamada; JAXA/TKSC: Atsushi Okamoto, Yoichi Sato, Keisuke Shinozaki, Hiroyuki Sugita; Chubu Univ.: Yoshiharu Namba; Ehime Univ.: Keiji Ogi; Kochi Univ. of Technology: Tatsuro Kosaka; Miyazaki Univ.: Yusuke Nishioka; Nagoya Univ.: Housei Nagano; NASA/GSFC: Thomas Bialas, Kevin Boyce, Edgar Canavan, Michael DiPirro, Mark Kimball, Candace Masters, Daniel McGuinness, Joseph Miko, Theodore Muench, James Pontius, Peter Shirron, Cynthia Simmons, Gary Sneiderman, Tomomi Watanabe; ADNET Systems: Michael Witthoef, Kristin Rutkowski, Robert S. Hill, Joseph Eggen; Wyle Information Systems: Andrew Sargent, Michael Dutka; Noqsi Aerospace Ltd: John Doty; Stanford Univ./KIPAC: Makoto Asai, Kirk Gilmore; ESA (Netherlands): Chris Jewell; SRON: Daniel Haas, Martin Frericks, Philippe Laubert, Paul Lowes; Univ. of Geneva: Philipp Azzarello; CSA: Alex Koujelev, Franco Moroso.

Appendix 1. The SXS PSF photometry analyses

When we apply the PSF photometry analyses to the SXS pixel map, we require that the satellite attitude is stable,

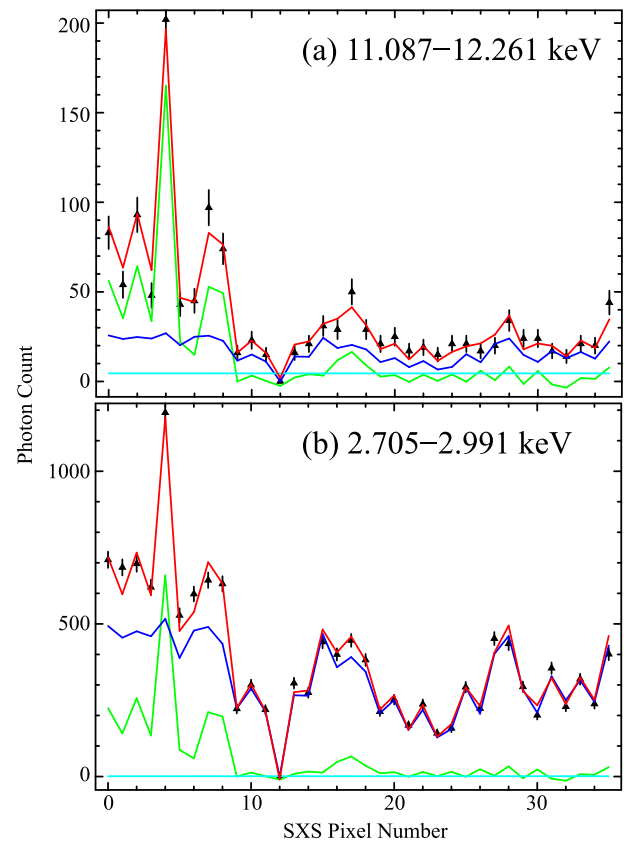


Fig. 6. SXS image fitting results of the 11.087–12.261 keV band (panel a) and the 2.705–2.991 keV band (panel b) in the PSF photometry method. The triangle data points show the photon count in each SXS pixel. Blue, green, and cyan represent the model components of ICM, AGN, and background, respectively, while red shows the total model. (Color online)

and hence we utilize the same GTI as used in sub-subsection 3.1.2. In detail, we create an SXS count map in 20 energy bands, where energy boundaries are logarithmically spaced in 2–15 keV. Because photon statistics in the higher energy bands are limited, we use wider energy bands above 15 keV: 15–17 keV and 17–20 keV. In addition, we apply finer energy bands around the Fe-K α line and Fe-K edge, avoiding the Fe xxv He α and Fe xxvi H α line complex: 6.0575–6.25, 6.25–6.26, ... (0.01 keV step); 6.32–6.33, 6.33–6.47, 6.62–6.78, 6.90–6.92, ... (0.02 keV step); 7.06–7.08; 7.08–7.41 keV. We then fit each count map with a spatial model consisting of ICM + AGN + background as shown in figure 6. The spatial distribution of the ICM in each band is assumed to follow that of the Fe xxv He α line complex (6.52–6.59 keV), with an iterative correction applied to account for the (small) contribution of the AGN to this band. Background counts are estimated from the public SXS background data, and then it is assumed to be uniform over all the SXS pixels.

In the estimation of the AGN emission spatial distribution, we create a spatial model by using the count map

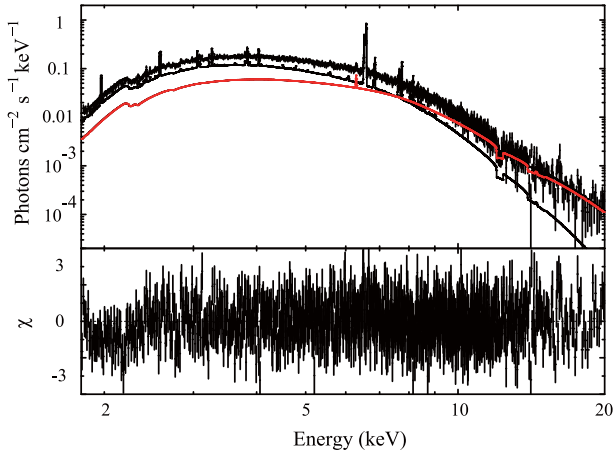


Fig. 7. As figure 5a except for the absence of the PSF photometry spectrum, but the AGN fitting parameters are limited within 90% errors which are derived in the fit to the PSF photometry spectrum. (Color online)

in 10–12 keV, and subtract the best-fit ICM emission and background model from the source image. In the count map fits, the AGN spatial model is not complete because of the PSF systematic errors and the attitude fluctuation, and hence the count maps are not well reproduced around the AGN. Therefore, we include the systematic errors to the estimated counts derived by the PSF photometry, so that the reduced χ^2 value of the count map fitting becomes 1. After fitting the SXS pixel map in each energy band, we calculate the model count rate of AGN in each energy bin in the center on-core nine pixels, and their errors are propagated from the image-fitting errors. As a result, we derive the PSF photometry spectrum of the AGN shown in red in figure 5.

Because the AGN continuum shape looks different between the direct fit to the SXS on-core nine-pixel spectrum and the PSF photometry spectrum fit as shown in figure 5a, the consistency between them should be checked. Thus, we fit the SXS on-core nine-pixel spectrum with the same model as in sub-subsection 3.2.1, but with the `pegpwr1w` photon index and the 2–10 keV flux limited to be free within the 90% error ranges derived by the PSF photometry spectrum fit (the Baseline column in table 4). Figure 7 shows the result, and the ICM emission parameters do not significantly change from those without the AGN parameter limitations (sub-subsection 3.2.1), as $z_{\text{ICM}} = 0.01729^{+0.00002}_{-0.00004}$, $T_e = 3.80 \pm 0.06$ keV, and $V_{\text{turb}} = 157.8 \pm 11.8$ km s^{−1}. The fit gives C-statistics/d.o.f. = 10568.6/11120, and its difference (Δ C-statistics) from the direct fit is only 6.4, which is statistically allowed. Thus, the PSF photometry spectrum is confirmed to be consistent with the AGN spectral shape derived by the direct fit in sub-subsection 3.2.1.

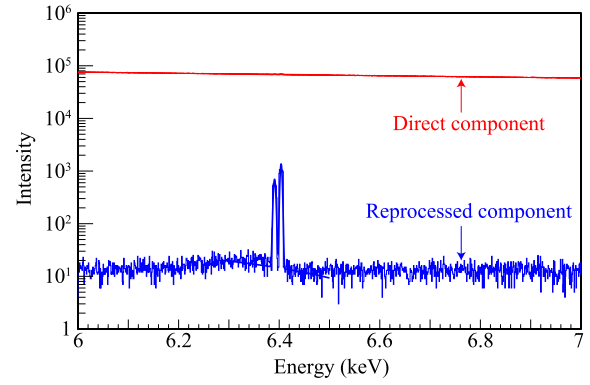


Fig. 8. The Monte Carlo simulation result using MONACO. Red shows the direct X-ray continuum, while blue represents a reprocessed emission including Fe-K α_1 and Fe-K α_2 lines. (Color online)

Appendix 2. Monte Carlo simulation

Usually, the fluorescence narrow and neutral Fe-K α line of AGN is thought to come from a BLR and/or a molecular torus. Estimation of such an Fe-K α line intensity has been reported by various authors (e.g., Ikeda et al. 2009; Murphy & Yaqoob 2009; Liu & Li 2014; Furui et al. 2016). However, the central dominant galaxy in the cluster of galaxies like NGC 1275 has other candidates for the fluorescence Fe-K α line source, as suggested by Churazov et al. (1998). Around NGC 1275, prominent H α filamentary structure and CO molecular clouds were reported (e.g., Salomé et al. 2006). When such CO clouds are illuminated by the AGN or the ICM X-ray continua, the fluorescence Fe-K α line can be generated. Thus, we employ Monte Carlo simulation to estimate the Fe-K α flux from the molecular clouds by utilizing the MONACO framework (Odaka et al. 2011; Hagino et al. 2015). The mass of each molecular cloud is set to be $10^9 \exp(-r/14) M_\odot$ against the distance r kpc from the NGC 1275 center, and the hydrogen number density is assumed to 10^3 cm^{−3}, which means that the typical cloud radius is $\simeq 0.2$ kpc. The radial distribution of clouds is calculated by differentiating the accumulated mass profile of $4.02 \times 10^9 \log(0.91 r) M_\odot$ with 5 kpc grids, and the clouds are placed spherically symmetrically with a random angular distribution. We assumed an intra-cloud velocity dispersion of $300-8 r$ km s^{−1} and a bulk cloud velocity of 200 km s^{−1} in random directions. All of the physical properties defined above are based on the observed cloud properties reported in Salomé et al. (2006).

The AGN input continuum spectrum is assumed to follow a power-law model with a photon index of 1.7. The ICM emission spectrum is assumed to follow a bremsstrahlung emission with a temperature of 3.8 keV, and the radial intensity distribution to follow a β model with a core radius of 26 kpc and a β of 0.53 (Zhuravleva et al. 2015). As shown in figure 8, the EW of the Fe-K α

line against the input continuum spectrum becomes 0.15 eV and 0.004 eV for illuminating sources of AGN and ICM, respectively. Thus, the Monte Carlo simulation with the MONACO framework revealed that the molecular clouds outside NGC 1275 generate too small Fe-K α flux to explain the EW of ~ 20 eV obtained by Hitomi/SXS, even when we consider the entire region of the 15 kpc filament.

References

- Abdo, A. A., et al. 2009, *ApJ*, 699, 31
- Aleksić, J., et al. 2012, *A&A*, 539, L2
- Angelini, L., et al. 2016, *Proc. SPIE*, 9905, 990514
- Antonucci, R. 1993, *ARA&A*, 31, 473
- Asmus, D., Hönig, S. F., & Gandhi, P. 2016, *ApJ*, 822, 109
- Balmaverde, B., & Capetti, A. 2014, *A&A*, 563, A119
- Balucińska-Church, M., & McCammon, D. 1992, *ApJ*, 400, 699
- Brenneman, L. W., et al. 2011, *ApJ*, 736, 103
- Canizares, C. R., et al. 2000, *ApJ*, 539, L41
- Cash, W. 1979, *ApJ*, 228, 939
- Churazov, E., Forman, W., Jones, C., & Böhringer, H. 2003, *ApJ*, 590, 225
- Churazov, E., Sunyaev, R., Gilfanov, M., Forman, W., & Jones, C. 1998, *MNRAS*, 297, 1274
- Eckart, M. E., et al. 2016, *Proc. SPIE*, 9905, 99053W
- Fabian, A. C., Rees, M. J., Stella, L., & White, N. E. 1989, *MNRAS*, 238, 729
- Fabian, A. C., Sanders, J. S., Taylor, G. B., Allen, S. W., Crawford, C. S., Johnstone, R. M., & Iwasawa, K. 2006, *MNRAS*, 366, 417
- Fabian, A. C., Walker, S. A., Pinto, C., Russell, H. R., & Edge, A. C. 2015, *MNRAS*, 451, 3061
- Fukazawa, Y., et al. 2011, *ApJ*, 727, 19
- Furui, S., Fukazawa, Y., Odaka, H., Kawaguchi, T., Ohno, M., & Hayashi, K. 2016, *ApJ*, 818, 164
- Gandhi, P., Hönig, S. F., & Kishimoto, M. 2015, *ApJ*, 812, 113
- Garmire, G. P., Bautz, M. W., Ford, P. G., Nousek, J. A., & Ricker, G. R., Jr. 2003, *Proc. SPIE*, 4851, 28
- Hagino, K., Odaka, H., Done, C., Gandhi, P., Watanabe, S., Sako, M., & Takahashi, T. 2015, *MNRAS*, 446, 663
- Hitomi Collaboration, 2016, *Nature*, 535, 117
- Hitomi Collaboration 2018a, *PASJ*, 70, 9 (V paper)
- Hitomi Collaboration 2018b, *PASJ*, 70, 10 (RS paper)
- Hitomi Collaboration 2018c, *PASJ*, 70, 11 (T paper)
- Hitomi Collaboration 2018d, *PASJ*, 70, 12 (Atomic paper)
- Hitomi Collaboration 2017, *Nature*, 551, 478 (Z paper)
- Ho, L. C., Filippenko, A. V., Sargent, W. L. W., & Peng, C. Y. 1997, *ApJS*, 112, 391
- Ichikawa, K., Ricci, C., Ueda, Y., Matsuoka, K., Toba, Y., Kawamuro, T., Trakhtenbrot, B., & Koss, M. J. 2017, *ApJ*, 835, 74
- Ikeda, S., Awaki, H., & Terashima, Y. 2009, *ApJ*, 692, 608
- Iwasawa, K., Fabian, A. C., Mushotzky, R. F., Brandt, W. N., Awaki, H., & Kunieda, H. 1996, *MNRAS*, 279, 837
- Kalberla, P. M. W., Burton, W. B., Hartmann, D., Arnal, E. M., Bajaja, E., Morras, R., & Pöppel, W. G. L. 2005, *A&A*, 440, 775
- Kawamuro, T., Ueda, Y., Tazaki, F., Terashima, Y., & Mushotzky, R. 2016, *ApJ*, 831, 37
- Kelley, R. L., et al. 2016, *Proc. SPIE*, 9905, 99050V
- Kilbourne, C. A., et al. 2016, *Proc. SPIE*, 9905, 99053L
- Kino, M., Ito, H., Kawakatu, N., Orienti, M., Nagai, H., Wajima, K., & Itoh, R. 2016, *Astron. Nachr.*, 337, 47
- Laing, R. A., Riley, J. M., & Longair, M. S. 1983, *MNRAS*, 204, 151
- Leutenegger, M. A., et al. 2016, *Proc. SPIE*, 9905, 99053U
- Liu, Y., & Li, X. 2014, *ApJ*, 787, 52
- Lodders, K., & Palme, H. 2009, *Meteorit. Planet. Sci. Suppl.*, 72, 5154
- McNamara, B. R., & Nulsen, P. E. J. 2007, *ARA&A*, 45, 117
- Minezaki, T., & Matsushita, K. 2015, *ApJ*, 802, 98
- Murphy, K. D., & Yaqoob, T. 2009, *MNRAS*, 397, 1549
- Nakazawa, K., et al. 2016, *Proc. SPIE*, 9905, 990511
- Nandra, K., & Pounds, K. A. 1994, *MNRAS*, 268, 405
- Nobukawa, K. K., et al. 2015, *ApJ*, 807, L10
- Odaka, H., Aharonian, F., Watanabe, S., Tanaka, Y., Khangulyan, D., & Takahashi, T. 2011, *ApJ*, 740, 103
- Okajima, T., et al. 2016, *Proc. SPIE*, 9905, 99050Z
- Porter, F. S., et al. 2016, *Proc. SPIE*, 9905, 99050W
- Pounds, K. A., Nandra, K., Stewart, G. C., George, I. M., & Fabian, A. C. 1990, *Nature*, 344, 132
- Ramos Almeida, C., & Ricci, C. 2017, *Nature Astron.*, 1, 679
- Reynolds, C. S., Nowak, M. A., & Maloney, P. R. 2000, *ApJ*, 540, 143
- Ricci, C., et al. 2017, *Nature*, 549, 488
- Salomé, P., et al. 2006, *A&A*, 454, 437
- Scharwächter, J., McGregor, P. J., Dopita, M. A., & Beck, T. L. 2013, *MNRAS*, 429, 2315
- Shu, X. W., Yaqoob, T., & Wang, J. X. 2010, *ApJS*, 187, 581
- Shu, X. W., Yaqoob, T., & Wang, J. X. 2011, *ApJ*, 738, 147
- Sikora, M., Stawarz, L., & Lasota, J.-P. 2007, *ApJ*, 658, 815
- Strüder, L., et al. 2001, *A&A*, 365, L18
- Takahashi, T., et al. 2016, *Proc. SPIE*, 9905, 99050U
- Tanaka, Y., et al. 1995, *Nature*, 375, 659
- Tavecchio, F., & Ghisellini, G. 2014, *MNRAS*, 443, 1224
- Tazaki, F., Ueda, Y., Terashima, Y., & Mushotzky, R. F. 2011, *ApJ*, 738, 70
- Tazaki, F., Ueda, Y., Terashima, Y., Mushotzky, R. F., & Tombesi, F. 2013, *ApJ*, 772, 38
- Tombesi, F., et al. 2016, *ApJ*, 830, 98
- Tsunemi, H., et al. 2016, *Proc. SPIE*, 9905, 990510
- Tujimoto, M., et al. 2018, *PASJ*, 70, 20
- Turner, M. J. L., et al. 2001, *A&A*, 365, L27
- Urry, C. M., & Padovani, P. 1995, *PASP*, 107, 803
- Watanabe, S., et al. 2016, *Proc. SPIE*, 9905, 990513
- Wilman, R. J., Edge, A. C., & Johnstone, R. M. 2005, *MNRAS*, 359, 755
- Yamazaki, S., et al. 2013, *PASJ*, 65, 30
- Yaqoob, T., George, I. M., Kallman, T. R., Padmanabhan, U., Weaver, K. A., & Turner, T. J. 2003, *ApJ*, 596, 85
- Zhuravleva, I., et al. 2015, *MNRAS*, 450, 4184